Journal of Alloys and Compounds 854 (2021) 157140

Contents lists available at ScienceDirect

Journal of Alloys and Compounds

journal homepage: http://www.elsevier.com/locate/jalcom

Multiscale mechanical performance and corrosion behaviour of plasma sprayed AlCoCrFeNi high-entropy alloy coatings

Ashok Meghwal [a], Ameey Anupam [a, b], Vladimir Luzin [c, d], Christiane Schulz [e], Colin Hall [e], B.S. Murty [b, f], Ravi Sankar Kottada [b], Christopher C. Berndt [a], Andrew Siao Ming Ang [a, *]

[a] *Surface Engineering for Advanced Materials (SEAM), Swinburne University of Technology, Hawthorn, VIC, 3122, Australia*
[b] *Department of Metallurgical and Materials Engineering, Indian Institute of Technology, Madras, Chennai, 600036, India*
[c] *Australian Nuclear Science & Technology Organisation (ANSTO), Lucas Heights, NSW, 2234, Australia*
[d] *School of Engineering, The University of Newcastle, Callaghan, NSW, 2308, Australia*
[e] *Future Industries Institute, University of South Australia, Mawson Lakes Campus, SA, 5000, Australia*
[f] *Indian Institute of Technology, Hyderabad, Telangana State, 502285, India*

ARTICLE INFO

Article history:
Received 10 July 2020
Received in revised form
16 August 2020
Accepted 9 September 2020
Available online 11 September 2020

Keywords:
High entropy alloys (HEAs)
Plasma spray
Nanoindentation
Wear
Residual stress
Corrosion

ABSTRACT

The combination of technical advantages of high entropy alloys (HEAs) and manufacturing capabilities of thermal spray (TS) offer potential towards new protective coatings to address extreme engineering environments. In this research, equi-atomic AlCoCrFeNi HEA coatings were synthesized *via* atmospheric plasma spray (APS) using mechanically alloyed feedstock, and a correlation between microstructure and mechanical properties in terms of both hardness and wear were established at multiscale levels. In addition, electrochemical performance in sea water and the overall residual stress distribution in the HEA coatings were also assessed. Superimposition of scanning electron micrographs and statistically analysed heat and contour maps using nanoindentation datasets revealed deviations in localized properties within and across individual phases; which were supported by Weibull plots of individual phases. Scanning wear tests revealed superior nanowear resistance of oxide phases developed by in-flight oxidation during APS process. In comparison, the HEA phases in the coating exhibited significant localized plastic deformation. The outcome of macroscale wear testing postulated that plasma sprayed AlCoCrFeNi HEA coatings exhibited superior wear resistance at high temperature (500 °C) than at room temperature, signifying high thermal stability of the coating. Residual stress generated due to plasma spray was measured using neutron diffraction and was tensile in nature. The corrosion resistance of the coating was slightly lower than that of SS316L, however, the anodic and cathodic polarization behaviour of HEA coating were identical to that of SS316L, indicating that the AlCoCrFeNi-based HEAs have prospects as corrosion resistant materials.

1. Introduction

High entropy alloys (HEAs) have been studied for more than a decade and are receiving attention due to their promising technological development in terms of compositions, processing routes and prospective applications. Solid solution alloys produced by combining five or more elements in equi- or near equi-atomic ratios is the most common compositional based definition used to define HEAs. In 2004, Yeh et al. [1] denoted such alloys as HEAs and in the same year Cantor et al. [2] termed them as multi-component alloys.

The stabilization of solid solution phases over complex intermetallics has been attributed to higher configurational entropy arising from multiple elements forming the lattice [2–4]. In addition, “cocktail effects” refer to the distinctive properties of HEAs due to collective interactions among all of the constitutive elements [4,5].

HEAs have shown potential for applications in extreme environments due to their attractive physical properties that arise from unique microstructures. Research shows that HEAs outperform

---

* Corresponding author. at: Faculty of Science, Engineering and Technology, Department of Mechanical Engineering and Product Design Engineering, Surface Engineering for Advanced Materials (SEAM), Swinburne University of Technology, H38, P.O. Box 218, VIC, 3122, Hawthorn, Australia.
E-mail address: aang@swin.edu.au (A.S.M. Ang).

https://doi.org/10.1016/j.jallcom.2020.157140

conventional materials in both room and high temperature properties, as well as at cryogenic temperature in terms of superior hardness [6–9], thermal stability [10–12], strength [13,14], fracture toughness [15–18], wear behaviour [19–21], electrochemical properties [22–24] and magnetic properties [25]. A major focus of the HEA community has been to tune and exploit the above properties by various synthesis routes to manufacture desirable microstructures. Thermal spray is one such process to generate thick coatings for demanding industrial environments.

The thermal spray process enables HEAs to be applied as coatings and the distinctive microstructure endows desirable physical and mechanical properties; for example, wear, corrosion and oxidation behaviour; and thermal stability under extreme environments, as summarized in a recent review [26]. The demand for novel protective coatings in extreme engineering environments has stimulated the development of thermal sprayed HEA coatings. HEAs have already exhibited potential to be competitive substitutes to conventional materials. One such HEA system is based on equiatomic AlCoCrFeNi, which has been widely examined due to its unique competences in terms of microstructure and mechanical properties. Within the thermal spray domain, equi-atomic AlCoCrFeNi HEA materials has been used as feedstock for plasma spray (PS) [27–30], high-velocity oxygen fuel (HVOF) [31] and cold spray [32] processes with the focus on microstructural, mechanical and oxidation property evaluations.

As reported in our previous studies [27,30], atmospheric plasma sprayed AlCoCrFeNi HEA possesses a composite microstructure with different alloy and oxide phases. A large disparity in their localized mechanical properties would affect the overall coating structure and integrity. Therefore, it is critical to formulate a connection between the multiphase microstructure and their localized mechanical properties. Nanoindentation is a widely accepted method to evaluate local mechanical properties of the materials [33] and has been used in the current study. The scanning wear module, available with nanoindentation, has evaluated the nanoscale wear behaviour of the coating with respect to the distinct phases within the coating. Within the frame of development of these coatings for extreme engineering environments, macroscale wear behaviour of the coating has also been analysed at room temperature and high temperature (500 °C). In addition, their electrochemical performance has been examined in sea water at room temperature and compared with conventional alloys.

Besides microstructure-mechanical property correlations, residual stresses in PS coatings also have a substantial influence on their mechanical properties. The temperature of the plasma generated is usually around 7000–20,000 °C, sufficient for melting all feedstock particles. The coating then builds up by surface adhesion of "splats" formed by rapid solidification of impacted molten feedstock particles on the substrate. The involvement of large temperature gradients and rapid solidification in the PS process lead to the development of residual stress in the coating [34]. Residual stresses generated due to the quenching stresses and differential thermal contraction stresses are driving forces for crack propagation and, lead to coating degradation [35]. Much of the research on residual stress measurements of PS coatings is restricted to hard metals or ceramic coatings. There is a lack of information on the quantitative measurement of residual stresses in AlCoCrFeNi PS HEA coatings.

This current work performs an extensive nano and microscale investigation of PS AlCoCrFeNi coating to correlate the microstructure-mechanical properties. An in-depth investigation into the localized mechanical properties of distinct phases formed during plasma spraying of AlCoCrFeNi HEA has been conducted. The mechanical properties have been analysed by means of ultrahigh-speed nanoindentation accelerated property mapping (XPM). A combined superimposition approach of microstructural and statistical analysis has been employed to characterize the variation in the properties among the different phases.

Table 1
Atmospheric plasma spray parameters for AlCoCrFeNi HEA coating [27].

Current (A)	300
Voltage (V)	65
Primary gas flow, Ar (slpm)	42.1
Secondary gas flow, H_2 (slpm)	2.35
Powder feed rate (g/min)	17 to 21
Powder carrier gas flow, Ar (slpm)	6
Stand-off distance (mm)	90
Nozzle type	GH

The residual stress profile of the coating has also been investigated experimentally using neutron diffraction. The study also focuses on multi-scale wear assessment of the coating, delineating complex wear mechanisms operating at different length scales, correlated with phase-specific wear behaviour. The collective contribution of these individual phases, which together form a composite, impacts the overall microstructure, properties and performance of the coating. Furthermore, the corrosion resistance of the coating has been evaluated in sea water solution and compared with conventional materials and other HEA TS coatings in literature.

2. Experimental procedure

2.1. Spraying procedure

Mechanically alloyed (MA) equiatomic AlCoCrFeNi HEA was thermal sprayed using a conventional atmospheric plasma spray system (Metco 7 MB, Sulzer Metco Inc., Westbury, NY). The synthesis of feedstock powder (AlCoCrFeNi HEAs) and spray process parameters was similar to those mentioned in previously by Ang et al. [27] and is represented in Table 1. The temperature of the substrate during plasma spraying was monitored using a thermocouple temperature logging device so that the thermal stresses due to differential cooling rates between substrate and coatings could be determined.

Two sets of coating samples were prepared: one series was sprayed on 3.0 mm thick stainless steel (SS316L) substrates and they were used for microstructural and mechanical characterization. The other series was sprayed on 3.2 mm thick copper substrates that were used for the neutron diffraction experiments to carry out a residual stress analysis.

2.2. Microstructural and mechanical characterization

Cross-sectioned samples for coating characterization were processed according to the ASTM E1920: Standard Guide for Metallographic Preparation of Thermal Sprayed Coatings [36]. Cross-section microstructural characterization was performed using a field emission scanning electron microscope (SEM) (Zeiss SUPRA™ 40VP FESEM system) with a working voltage of 5 kV and working distance of 9 mm. An energy dispersive X-ray spectrometer EDS (Oxford Instruments, INCAxcat detector) allowed point scanning of element distributions. X-ray diffraction patterns were replotted as per the previous reports [27,30] and, further analysed in DIFFRAC. SUITE TOPAS 4.2 (Bruker Corp., Billerica, MA, USA) to compute the lattice parameters and phase contents in both powder and coating using quantitative Rietveld analysis method.

Microindentation was performed using a Hysitron TI 980 Triboindenter under a load of 300 g applied for 15 s. Thirty indents were taken across the cross section of the AlCoCrFeNi coating to determine their mechanical response in terms of microhardness and elastic modulus.

For the PS AlCoCrFeNi HEA coating, nanoindentation was performed with a cube conical diamond tip on a Hysitron TI 980 Triboindenter. An XPM testing function is incorporated into Hysitron's Triboscan control and data analysis software package. In XPM, an array of indents can be arranged spatially with a specific indentation load onto the desired area within the microstructure, which is located by using both optical and *in-situ* scanning probe microscopy (SPM) that is part of the Hysitron Triboindenter. Testing in XPM mode can be accomplished 500 × faster than conventional nano-mechanical testing. An indentation matrix of 6 × 6 with 36 indents per map, within an area of $50 \times 50\ \mu m^2$, at a maximum load of 5000 μN was executed using nanoindentation XPM accelerated property mapping. Nine such matrices were created over the whole coating cross-section. A spacing of 8 μm between indents prevented the indent impressions from confounding the individual data points. Post-indent SEM was performed to observe the indentation impressions within individual phases. Any interfacial indent measurements were excluded from analysis. The data sets were assessed by Weibull statistical analysis.

The Oliver and Pharr method measures a series of load-displacement data sets, with fitting the initial unloading curve to the derivative of the Hertz equation to evaluate the hardness and elastic modulus [37]. This method is less erroneous due to analysis of an array of unload points and, moreover, can be implemented without using a microscope to image the residual indent for the calculation of hardness [38,39]. The nano-indentation hardness, H, and reduced elastic modulus, E_r, derived from Oliver and Pharr method are determined as follows:

$$H = \frac{P_{max}}{A_C} \tag{1}$$

$$E_r = \frac{\sqrt{\pi}}{2}\frac{S}{\sqrt{A_C}} \tag{2}$$

where, P_{max} is the maximum load applied (in μN), A_c is the projected contact area (in nm^2) and S is the contact stiffness (in μN/nm). With the assumption of using an ideal cube-corner indenter as for the current study, the projected contact area is equivalent to $2.60h_c^2$ with h_c being the contact depth (in nm) between indenter and the sample.

Origin Pro (Origin 2019b, OriginLab Corp., MA) was used for data analysis to develop contour and heat maps of hardness for each matrix. A heat map is a two-dimensional graphical demonstration of data in which different values are visualised in different colours. Superimposition of SEM micrographs, nanoindentation *in-situ* scanning probe micrographs (SPM), and statistically analysed heat and contour maps revealed deviations in localized properties as well as variations within individual phases. Weibull statistical analysis allowed comparison of hardness distributions among the phases observed in the coating.

The same nanoindentation equipment was also used for nanowear analysis using scanning wear testing with *in-situ* SPM imaging mode. In scanning wear tests, the indenter tip is raster scanned over the polished sample surface ($R_a = 0.02\ \mu m$) for a given number of passes to create the wear regions. Wear volume can be calculated by multiplying the scanned area size to the height difference between pre- and post-scanning surfaces. Before conducting the scanning wear test, the desired areas within APS AlCoCrFeNi HEA coating were first identified using SEM. These areas were further mapped using *in-situ* SPM imaging mode to enable the direct measurement of the surface morphology. Hysitron Triboindenter has integrated *in-situ* SPM, which uses the same probe to image the specimen surface under a load of 2 μN and scanning frequency of 0.8 Hz, keeping the sample stationary. Scanning wear tests were conducted using a cono-spherical 1 μm diameter diamond tip under a load of 300 μN across an area of $10 \times 10\ \mu m^2$. Each area was scanned with 3 passes at a scanning frequency of 0.8 Hz. A total of 4 areas were analysed to calculate the average nanowear of the coating surface and to accurately analyse the localized wear characteristics of individual coating phases. After scanning wear testing, the worn surface was scanned by *in-situ* SPM using the same tip over a $20 \times 20\ \mu m^2$ area. The line scan and contour profiles of worn area were plotted using Origin Pro (Origin 2019b, OriginLab Corp., MA).

Wear testing was performed using a pin-on-disc tribometer (Microtest, S.A., Spain) with a 6 mm diameter Al_2O_3 ball against the flat coating sample. The top surface of coating samples was polished to 1200 grit and cleaned with ethanol before wear testing. The tests were executed at room temperature (25 °C) and 500 °C (denoted as RT and HT, respectively). Three wear tests on each coating sample were conducted at 10 N load to obtain the average volume loss of materials at both temperatures. The sliding distance was 1000 m, at a speed of 0.52 m/s, with a 10 mm wear-track diameter. For HT tests, the sample temperature was stabilized to 500 °C before starting the experiment. In order to estimate the volume loss of the coating, laser confocal microscopy (LEXT OLS5000, Olympus, Japan) was used to scan the wear area of the materials followed by volume loss analysis through Lext software. Wear track surface and wear debris were further analysed using SEM and EDS and surface topographical images were acquired using a 3D optical profilometer (Bruker Corporation, Billerica, MA, USA). The chemical composition of the HT worn surface was analysed using an X-ray photoelectron spectrometer (XPS) with a Kratos Axis Ultra DLD spectrometer. The XPS data were analysed by CasaXPS software (Version 2.3.15, CASA Software Ltd., Cheshire, UK) with the correction of binding energy for carbon at 284.8 eV.

2.3. Electrochemical analysis

The electrochemical performance of the coating was evaluated in filtered sea water with a conventional three-electrode cell system using a PARSTAT 2273.02 potentiostat (Princeton Applied Research) at room temperature. The polished surface (1200 grit) of both coating sample and uncoated substrate SS316L with surface area 1 cm^2 were used as working electrodes. The reference electrode was Ag/AgCl in a saturated KCl solution. Two parallel graphite rods were employed as the counter electrode. The open circuit potential (OCP) was measured for 60 min prior to electrochemical testing to obtain the steady state potential. The potentiodynamic polarization test was conducted at a scan rate of 1 mV/s from an initial potential −0.5 V to a final potential of 1.5 V against the OCP. The experiment was repeated three times to ensure repeatability.

2.4. Neutron diffraction residual stress measurement

Residual stresses of plasma sprayed AlCoCrFeNi HEA coating on copper substrates were measured by neutron diffraction technique using KOWARI [40], which is the neutron residual stress diffractometer at the Australian Centre for Neutron Scattering (ANSTO). The basics of the neutron diffraction experimental setup, experimental procedure and data analysis in the case of substrate-coating systems are given in details elsewhere [41,42]. Other specific experimental parameters for the HEA samples are reported below.

Since the substrate thickness was 3.2 mm, the through-thickness stress profile was measured with high spatial resolution

(0.2 mm in the through-thickness direction) at 0.2 mm steps. Due to the possibility of using match-stick gauge volume for the planar sample geometry, the overall gauge volume of 0.2 × 0.2 × 20 mm^3 was sufficient for fast (10 min per point) and accurate (50 µstrains) measurements on the Cu substrate. The elastic strain were derived from analysis of the shift of the strongest Cu (311) reflection measured at 90°-geometry using neutron beam with wavelength of 1.55 Å. Residual strains were quantified in the two principle directions: in-plane and normal, assuming an equi bi-axial stress state that was demonstrated in similar coating systems [41,43]. The stresses were recalculated from strain using hkl-dependent X-ray elastic constants: $S1 = -2.88\ TPa^{-1}$ and $S2 = 11.06\ TPa^{-1}$. They were evaluated in the quasi-isotropic approximation from the single crystal elastic constants of copper using IsoDEC software [44].

Measuring the coating material in the same neutron diffraction setup, with the same resolution, was not practical due to several complications. First, intensity of the HEA diffraction peak, even the strongest HEA (311), was relatively low; approximately 10 times lower than Cu (311). Second, a strong overlap between Cu (311) and HEA (311) prevented performing high accuracy positioning and the peak fitting routine could not provide a good accuracy of strain even for long measurement times. Potentially reducing the spatial resolution to 0.1 mm might have benefited the positioning procedure, but this would further reduce the intensity with no practical value to the overall stress analysis of the coating material. Third, with the evidence that the coating material is multiphase, the experimental difficulties are more challenging with the necessity to measure all phases with low volume fraction and with high resolution. Fourth, even though there are no measurements for coatings, the overall stress in coatings can be derived indirectly on the basis of accurate measurements in the substrate. The macrostress or phase-averaged stress can then be calculated by considering the force and bending moment balance conditions. This method was confirmed in previous experiments on thin coatings [45].

In the current coating system, the stresses induced from the grit-blasting process were included into the stress analysis on the basis of the model approach of Tsui & Clyne [46]. The grit-blasting induced residual stress in the substrate exhibited the typical distribution of a compression zone to the depth of less than a millimetre from the surface/interface. This grit-blast residual stress can be characterized by several parameters such as intensity and width, which can be included into the fitting procedure.

3. Results and discussion

3.1. Microstructural characterization

XRD patterns of AlCoCrFeNi powder mechanically alloyed (MA) for 10 h, and plasma sprayed AlCoCrFeNi coating, which were reported in previous studies [27,30], are replotted with the additional Rietveld fitting using the TOPAS 4.2 user interface in Fig. 1. As reported earlier, MA powder was composed of major BCC (marked as B) and minor FCC (marked as F) phases. Rietveld analysis was used to calculate the lattice parameters and weight fractions of the phases, (Table 2), and revealed that both the BCC and FCC phases had similar phase fractions, at 52 and 48 wt%, respectively. It must be noted that after 10 h of MA, only alloy BCC and FCC phase peaks were observed, and no undissolved elemental peaks were detected; implying that alloying is complete. In contrast, for the same composition, Ji et al. [47] reported a single phase BCC after 60 h of MA; while Vaidya et al. [48] report that at least 15 h of MA is required to dissolve all elemental peaks. It is noted that there are slight variations in the milling parameters reported in the literature, demonstrating the sensitivity of phase formation in this HEA composition processed by this route.

We report BCC phase with a calculated lattice parameter of 2.87 Å, and FCC phase with lattice parameter of 3.57 Å. Based on phase evolution studies carried out by Vaidya et al. [48], it is evident that the BCC phase formed initially is Fe–Cr based. Additionally, Ni and Co tend to stabilize the FCC phase. Al is a known BCC/B2 stabilizer owing to its negative mixing enthalpy with Co, Ni and Fe. There is thus the possibility that the BCC phase observed after 10 h of MA is composed of two BCC phases – one Al–Ni rich (B2) and the second, Fe–Cr rich BCC, with very close lattice parameters, making them difficult to resolve in XRD. These phases have been detected in as-cast AlCoCrFeNi as decomposed at nanoscale, while the XRD showed only a single-phase BCC [49]. The FCC phase is expected to be Ni–Co–Cr based, and lean in Al. The three phases are still comprised of five elements in non-minor quantities. Perhaps milling for longer duration would stabilize the BCC phase, but it would also accrue contamination from the milling medium (WC), which is undesirable.

XRD analysis of the APS coating revealed FCC and BCC as the major phases. A second minor BCC phase (marked as B’) with a slightly different lattice parameter than the dominant BCC was also detected. In addition, due to in-flight oxidation (IFO) characteristic of APS process, peaks of mixed spinel oxides (marked as S) AB_2O_4 (A = Ni/Co/Fe, B = Al/Cr) were also observed. The lattice parameters and weight fraction calculated using Rietveld analysis in TOPAS 4.2 of APS coating are also presented in Table 2. During APS, HEA particles (composed of up to 3 phases) experience melting and varying degrees of in-flight oxidation, as discussed by Anupam et al. [30].

The major FCC phase (68 wt%) in the APS coating stems from (i) the original Ni–Co based FCC in MA AlCoCrFeNi; (ii) Al-depleted $Al_xCoCrFeNi$ ($x < 0.5$) (from the previously Al-rich B2/BCC phase after IFO); and (iii) the Fe/Cr based second BCC phase, which lost some Fe, Cr to IFO. The FCC phase fraction increases from 48 wt% in MA powder to 68 wt% in APS due to the additional contribution from the new Al-depleted phases. The BCC phase corresponds to the unoxidized HEA phase that is retained in the coating. The drastic difference in the BCC phase fractions in the MA and APS XRDs (52 wt% vs. 8.5 wt%) bears testimony to the high reactivity of these nanocrystalline powders to an oxidizing environment. The B’ (BCC) phase, with a lattice parameter of 2.98 Å and weight fraction of 1.53% could be a residual alloy phase. However, phases below 5% weight fraction cannot be detected by XRD, and this measurement could be an aberration. The mixed oxide phase peaks, although grouped under one heading, are actually composed of multiple oxides; of the AB_2O_4 type such as $NiCr_2O_4$, $FeAl_2O_4$, etc., derived from different degrees of oxidation of the various alloy phases during APS.

As reported earlier [27], cross-sectional SEM (Fig. 2) of APS AlCoCrFeNi HEA coatings reveal the presence of three phases with different atomic number (z) contrasts; (i) grey (denoted as G), (ii) white (denoted as W), and (iii) black (denoted as B), forming a homogenous composite layered structure. Energy dispersive spectroscopy (EDS) point analysis of individual phases specifies that ‘B’ phase is rich in aluminium and oxygen; however, these phases do not appear in XRD owing to their lower content. Phase ‘G’ refers to Al–Cr–Fe rich oxide, which are essentially the mixed oxides detected in XRD. The ‘W’ phase shows depletion in Al content with a low oxygen level, resulting in an aluminium depleted multicomponent HEA, i.e., the FCC + BCC phases from XRD.

In our recent work [30], extensive advanced microstructural characterization of an APS AlCoCrFeNi HEA coating discovered the presence of multiple alloy phases with various compositions within the W phase; both AB_2O_4 (A = Ni, Co, Fe; B = Al, Cr) and complex HEA oxide phases within the G phase; and $(Al,Cr)_2O_3$ oxides within

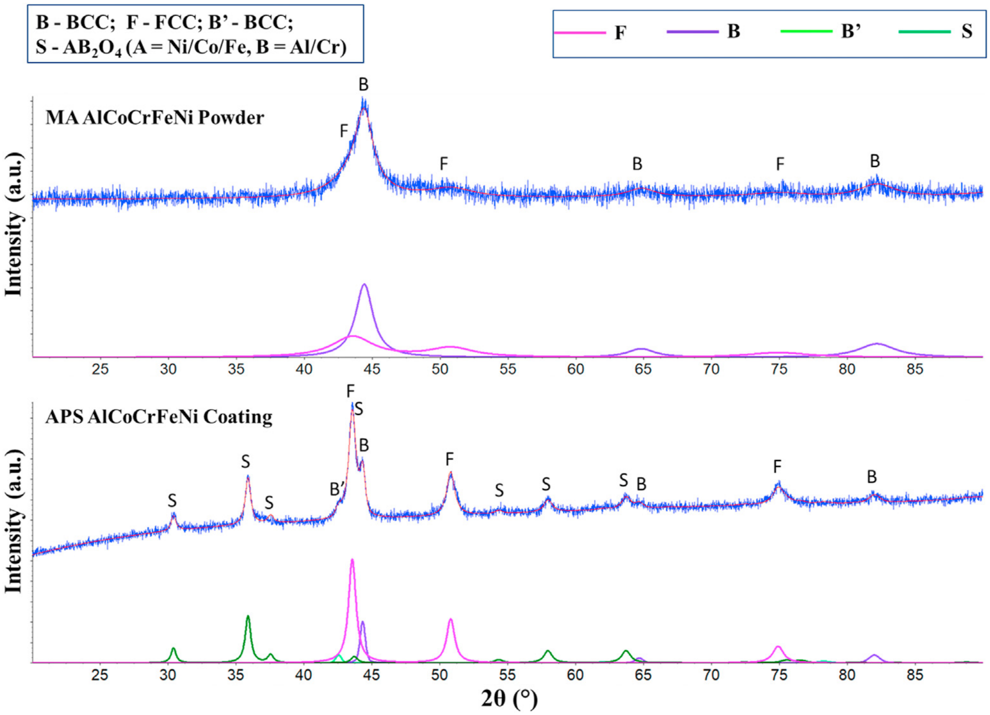

Fig. 1. Rietveld analysis peak fitting of the phases observed in the XRD patterns of the mechanically alloyed AlCoCrFeNi powder and atmospheric plasma sprayed AlCoCrFeNi HEA coating.

Table 2
Lattice parameters and phase content of the constituent phases of the atmospheric plasma sprayed AlCoCrFeNi HEA coating.

	Phase	Lattice parameter (Å)	Phase content (wt.%)
Powder	BCC (B)	2.87 ± 0.25	51 ± 3
	FCC (F)	3.57 ± 0.31	48 ± 3
Coating	FCC (F)	3.57 ± 0.01	68.2 ± 0.6
	BCC (B)	2.87 ± 0.01	8.5 ± 0.4
	BCC (B′)	2.98 ± 0.01	1.5 ± 0.4
	AB_2O_4 (S)	8.28 ± 0.03	21.7 ± 0.5

the B phase of the coating. Since our focus is on an in-depth mechanical analysis of APS AlCoCrFeNi HEA coating, and the nanoindentation technique used here is limited in terms of the test area observed by optical microscopy, the easily perceivable z-contrast between phases has been used as the main differentiator.

3.2. Micro- and nanoindentation analysis

The Vickers hardness of AlCoCrFeNi coating was 4.13 ± 0.43 GPa (HV300gf, n = 30), which was higher than that for supersonic APS AlCoCrFeNi (1.7 GPa) [28] and cold sprayed AlCoCrFeNi coatings (3.8 GPa) [32]. This can be attributed to the additional strengthening of the alloy phases with relatively harder oxide phases generated by IFO. The elastic modulus of coating was measured as 106 ± 7 GPa and used in calculating the coating thermal stresses.

Nanoindentation is the appropriate technique for analysis of nanomechanical properties of multi-phase APS AlCoCrFeNi HEA

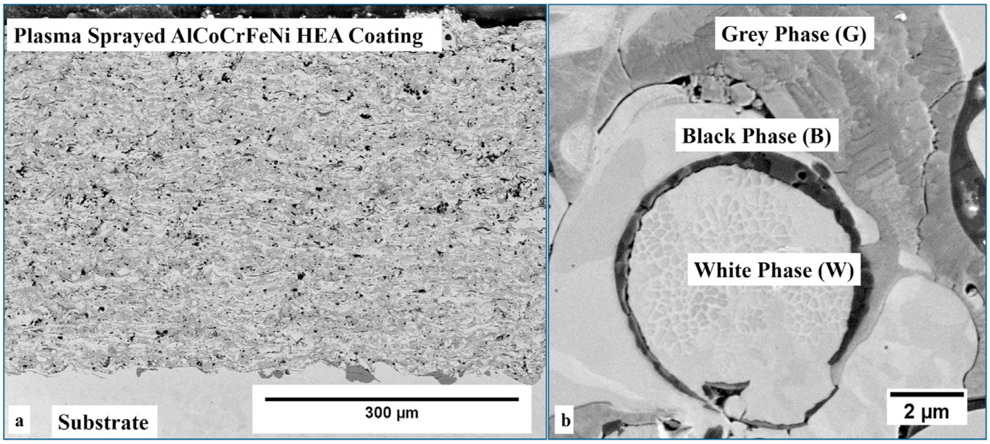

Fig. 2. Cross-sectional SEM micrograph of (a) plasma sprayed AlCoCrFeNi HEA coating, (b) high magnification image showing distinct contrast between Grey (G), White (W) and Black (B) phases.

Table 3
Average contact depth (in nanometers), reduced elastic modulus, E_r (in GPa), hardness, H (in GPa) values with their standard deviation and coefficient of variation (CV), H/E_r and H^3/E_r^2 ratios measured during nanoindentation of individual phases observed in AlCoCrFeNi coating.

ID	Phases	Number of Indents (n)	Contact Depth, h_c (nm)	Reduced Elastic Modulus, E_r (GPa)	CV Reduced Elastic Modulus (%)	Hardness, H (GPa)	CV Hardness (%)	H/E_r	H^3/E_r^2
B	Al-rich Oxide (Black)	25	243 ± 119	162 ± 42	26	15 ± 9	57	0.093	0.125
G	Al–Cr–Fe rich Oxide (Grey)	88	239 ± 71	151 ± 28	19	13 ± 5	37	0.083	0.086
W	Al depleted HEA (White)	107	430 ± 104	142 ± 31	22	5 ± 2	34	0.037	0.007

coating. Each of the indentation matrices of 6 × 6 indents was observed under SEM to locate each indent on individual phases, followed by an evaluation of their nanomechanical properties. Table 3 lists the results of contact depth (in nanometers), reduced elastic modulus, E_r (in GPa) and hardness, H (in GPa) for the three phases (white (W), grey (G) and black (B)). The average hardness and average reduced elastic modulus for all 324 indents was 9 ± 6 GPa and 153 ± 33 GPa, representing a coefficient of variation, CV, of 63% and 21%, respectively.

Fig. 3(a) and Fig. 3(b) show the SEM images of nanoindent impressions on the individual G, W and B phases. Fig. 3(c) represents the load-depth curves corresponding to phase-wise indents as indicated in Fig. 3(a) and (b). Under identical loading conditions (5000 μN), for an average of 25 indents per phase, the indentation depth for B was found to be lowest, followed by G, and W. This implies that phase B (alumina) is harder and more resilient to plastic deformation, than G (mixed oxides); while W (alloy) is the softest phase. The higher indentation depth and wider indent impression for the softer phase W (Fig. 3(a) and (b) and Table 2) substantiate these results. Thus, there is a significant difference in hardness distribution for different phases. This variation in nanohardness with the indentation depth is associated with the indentation size effect (ISE), which implies that a decrease in indent size corresponds to both an increase in hardness and decrease in plasticity [50]. The variation in reduced elastic modulus is not as radical as hardness, as evident from the lower CV values shown in Table 3.

The wider impression of the white phase (W) also exhibited material pile-up around the indents, see Fig. 3(a). The appearance of material pile-up during nanoindenation has been attributed to highly localized plastic deformation of the phase [51,52]. Further, the ratio H^3/E_r^2 signifying the material's resistance to plastic deformation, was found to be lowest in the case of the white phase (Table 3). A simulation study conducted by Muthupandi et al. [52] predicted that nanoindentation of material with low H/E_r ratio results in pile-up along the indent due to progression in plasticity and proliferation of the plastic strain across the indenter tip. The observed low H^3/E_r^2 ratio and material pile up around indents in the W phase conformed to this behaviour.

Weibull plots assessed the hardness variability of B, G, and W phases, as shown in Fig. 4(a). The Weibull modulus (m) measures the distribution of flaws; the R^2 value measures the goodness of fit; and n represents the number of indents. A higher Weibull modulus indicates a lower CV in hardness values [27,53], implying greater uniformity in property distribution. The "m" values for the B, G and W phases were 1.7, 3.0 and 3.4, respectively. Note that although the B phase possesses the highest average hardness, it also displays the largest variation in hardness compared to the other two phases. This could arise from compositional variations due to varying oxidation kinetics and solidification rates operating during thermal spray [30].

Melting and oxidation of HEA feedstock powders during spraying resulted in generation of multiple alloy and oxide phases with varying chemistries. The hardness values of both oxide phases (B and G) are within the error range of each other, implying differences arising from oxide chemistries and crystal structures. It is established in bulk HEA literature that Al is a BCC/B2 stabilizer and improves the alloy hardness/strength [7]. However, in the present case, Al depletion from the alloy during IFO results primarily in Al-lean CoCrFeNi type FCC phases, which are much softer (570 HV1 as reported by Praveen et al. [54]) than the oxide phases.

In comparison to nanoindentation, the Vickers hardness and elastic modulus obtained for APS AlCoCrFeNi coating were 4.13 ± 0.43 GPa and 106 ± 7 GPa, respectively. As expected, nanohardness measured at relatively low load (5000 μN) exhibited higher values than Vickers hardness, which was measured at higher load (300 g-force = 2.94 N). This difference can be attributed to the ISE, wherein the generation of strain fields under the smaller indent areas lead to dislocations that are responsible for the higher hardness. The Weibull moduli were 9.2 and 2.2 for micro and nanohardness, respectively (Fig. 4(b)). The high "m" arising from Vickers hardness establishes its reliability as a hardness measurement technique. This bulk measurement, however, confounds the nanomechanical properties. The Vickers indentation impression of a typical 31.50 μm diagonal encompasses a volume of ~908 μm^3. This macroscopic volume includes many phases, porosity and microstructural defects that develop due to the spray process, as shown in Fig. 3(d). Thus, the calculated hardness is the balance of many microstructural artefacts that are confined under the Vickers indent. On the other hand, Fig. 3(a) illustrates that nanoindentation is minimally affected by such defects due to (i) the small indent size with less volume tested (approximately 0.63 μm^3) and (ii) precise indent positioning [55,56]. Hence, the volume of the nanoindentation probe is focused on a specific phase and its hardness can be directly measured. The high variation in hardness values for nanoindentation verifies that nano-hardness values depend on individual phase structures, their compositions and positioning of the indent within the microstructure.

3.3. Microstructure-mechanical properties correlation

Hardness contour and heat maps were developed using data analysis and graphing software by Origin Pro 2018b. Fig. 5 shows the superimposed heat map of a 6 × 6 indent matrix upon the post-indent SEM image. The B, G and W letters mentioned in Fig. 5 specify the indents located precisely on Black, Grey and White phases, respectively. The indent data points are colour coded according to their values. Superimposition of the hardness heat map onto the post-indent SEM image in Fig. 5 reveals that the hardness distribution at the nano-scale is inhomogeneous throughout the coating microstructure.

Microstructure-mechanical property mapping is depicted in Fig. 6 where the hardness and reduced elastic modulus contour map is laid over the post-indent SEM image. Nanoindentation mapping was performed for a matrix of 6 × 6 indents (36 indents) within an area of 50 × 50 μm^2 using the XPM technique. Initially,

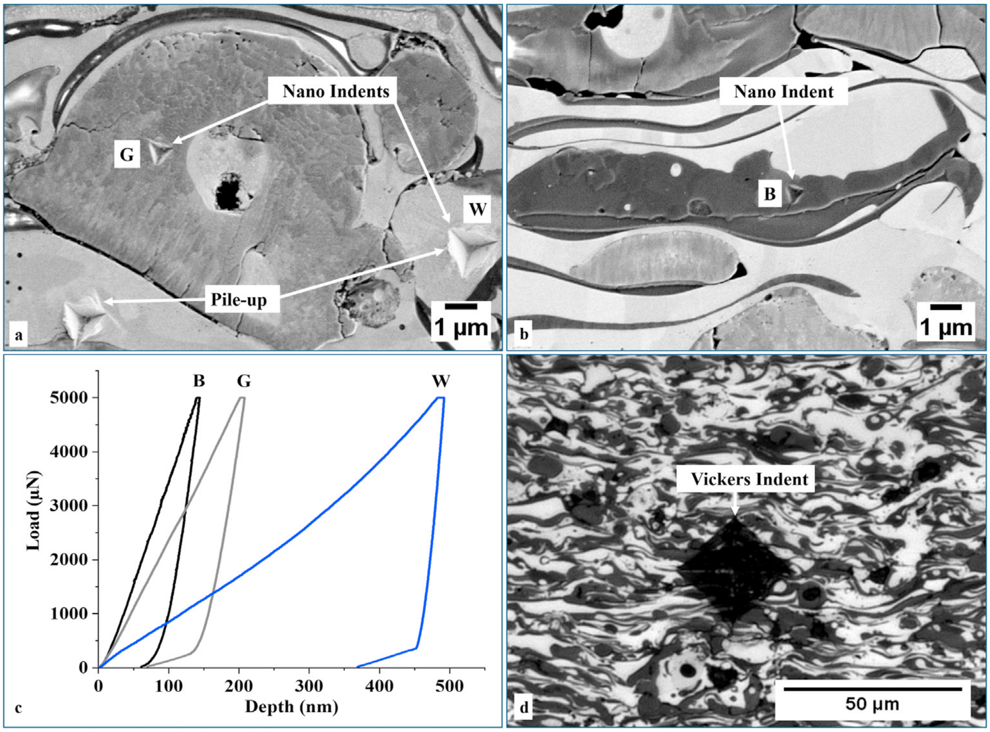

Fig. 3. (a) Precise nanoindentation impressions on G and W phases and pile-up around the indent of W phase imaged by SEM, (b) indent impression on B phase, (c) load-depth curve of the corresponding indent impressions of G, B and W phase mentioned in (a) and (b) and, (d) Vickers indentation impression covering a large volume of the microstructure, including multiple phases, porosity and microstructural defects imaged *via* optical microscopy.

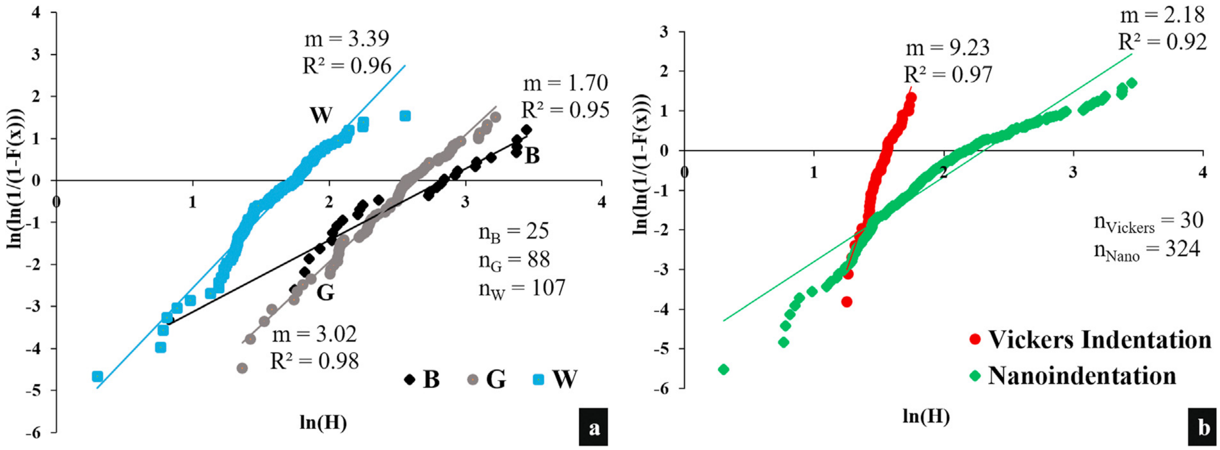

Fig. 4. (a) Weibull plots showing variability in nanoindentation hardness within three phases (B, G and W) observed in plasma sprayed AlCoCrFeNi coating, and (b) Weibull plots comparing hardnesses between Vickers indentation and the pooled nanoindentation data.

the area of interest focused on a region where the three phases were observable under SEM. The identical area was identified through *in-situ* SPM imaging. After nanoindentation, the area was scanned using *in-situ* SPM to capture the post-indentation image (Fig. 6(a)); which was followed by post-indent SEM (Fig. 6(b)). A hardness contour map was coupled with the hardness values and superimposed on the post-indent SEM image (Fig. 6(c)). A similar model was followed for reduced elastic modulus mapping (Fig. 6(d)). Superimposing the images revealed the correlation between microstructure and mechanical properties at local levels. The hardness and reduced elastic modulus variation among different phases is distinctly revealed and the influence at phase boundaries is noticeably visible.

Fig. 6(a) is an *in-situ* SPM image of the coating cross section after indentation has been carried out. The image contrasts correspond to topological variations in the surface where the hills and valleys correspond to harder and softer phases, respectively; and which are created by preferential polishing of the softer phase. This is thus a qualitative indicator of the hardness differences of the various phases. On the other hand, Fig. 6(b) is the BSE-SEM image delineating the identity of the various phases in the coating. BSE-SEM after XPM mapping is vital for identifying the exact location of the indents: that is, whether they fall completely within a phase, or at a phase interface. This is important because, (i) in the former case, the nanohardness can be attributed to that specific phase, while (ii) in the latter case, the nanohardness value is akin to a

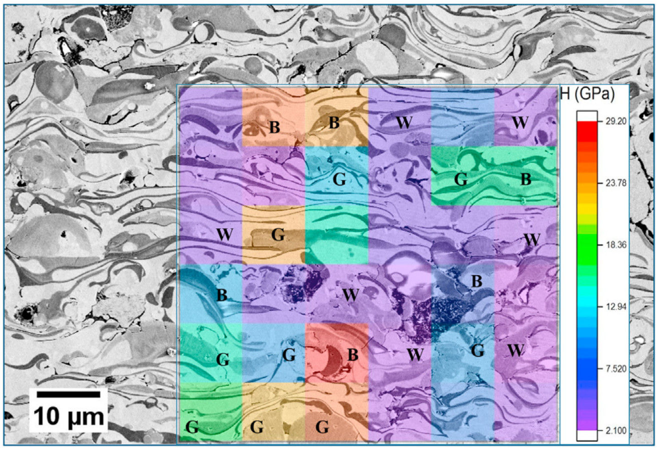

Fig. 5. Superimposition of statistically analysed heat map on post-indent SEM image of an indentation matrix of 6 × 6 indents to reveal variability in hardness distribution at the local level among different z-contrast phases denoted as B, G and W.

weighted average of the two phases, depending on the area of the indent falling on either side of the phase boundary. These three features (SPM, BSE-SEM and XPM) are combined to develop XPM maps shown in Fig. 6(c) and (d) for nanohardness and reduced elastic modulus, respectively.

Hardness measured by nanoindentation is a function of the sample material response only (equation (1)), whereas E_r incorporates compliance from the indenter (equation (2)). For this reason, the nanohardness value distinguishes between the alloy and oxide phases within the APS-HEA coating (Fig. 6(c)). Calculation of E from the E_r values depend on the Poisson's ratios of the respective phases, which can only be estimated. For this reason, the E_r map looks largely homogeneous (Fig. 6(d)), whereas nanohardness maps identify regions rich in alloy or oxide splats. As it was stated in an earlier section, B phase possesses higher hardness compared to G and W phases due to oxide formation, crystal structure and chemistry (Fig. 6(c)). In contrast, the reduced elastic modulus showed little difference with respect to the different phases; but follows a similar pattern as hardness mapping at the coating defect location (Fig. 6(d)). More importantly, microstructure-mechanical property mapping demonstrates the transition of hardness at the phase interface, which follow a step-by-step decrement instead of a rapid change (Fig. 6(c)).

There is also an inherent issue of differences in resolution offered by XPM concerning the size and irregular shape of the microstructural splats in the coatings. As mentioned earlier, a spacing of 8 μm was maintained between indents to avoid overlap between neighbouring indents. Therefore, the contouring function must interpolate values between the two measured data points. As learned recently from Phani et al. [57], the inter-indent spacing can be safely reduced further; hence the resolution of XPM maps for such microstructures may be improved.

The microstructure-mechanical property mapping technique precisely evaluates the localized disparity in properties which, in conjunction with statistical analysis, uncovers mechanical property-microstructural relationships that are obfuscated by traditional Vickers indent methods. The mapping technique boosts both the resolution limit and functionality of the nanoindentation test. A matrix of indents can be spatially arranged over the desired microstructure and variability in mechanical properties across the microstructure can be determined using statistical analysis.

3.4. Residual stress profiling

The main contributors to residual stresses resulting due to the

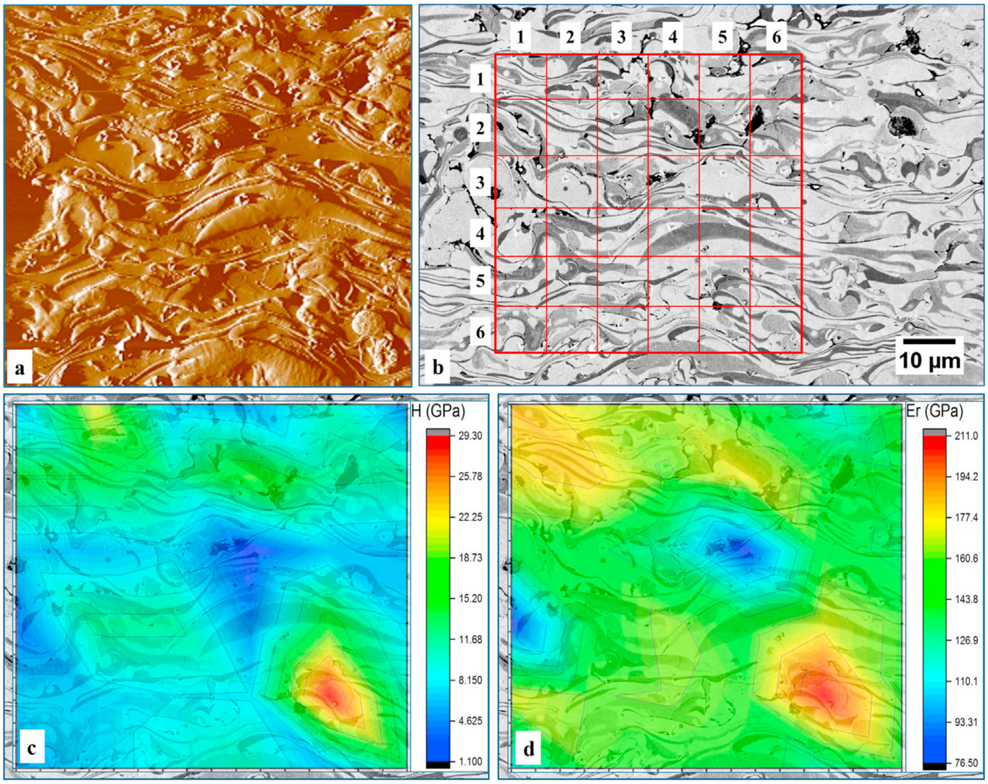

Fig. 6. (a) Post-nanoindentation mapping image obtained by *in-situ* scanning probe microscopy, (b) post nanoindentation mapping SEM image, and (c, d) superimposition of the contour map over the post-indent SEM image to show variation in hardness and reduced elastic modulus across and within different phases.

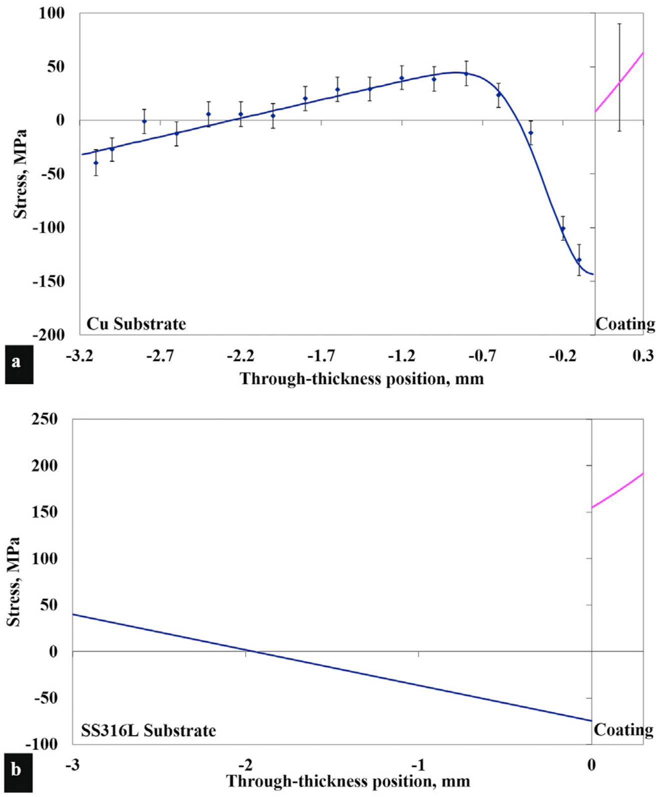

Fig. 7. (a) Through-thickness stress profiles of plasma sprayed AlCoCrFeNi HEA coating measured by neutron diffraction for the 3.2 mm copper substrate. The experimental data points are shown as symbols, while lines represent model profiles that fit the experimental data; **(b)** Through-thickness stress profiles of plasma sprayed AlCoCrFeNi HEA coating calculated for the 3.0 mm thick SS316L substrate. The conventions of the plots are the same as those in Fig. 7(a).

plasma spray process can be attributed to: (i) quenching (compressive deposition stress), and (ii) differential thermal contraction (between the substrate and coating). The quenching or intrinsic stresses arise due to the hindered shrinkage of individual molten splats as they undergo rapid solidification. The substrate is usually maintained at an elevated temperature during coating deposition. On cooling, differences between the thermal expansion coefficients (CTE) of the deposit and the substrate generate a second contribution to the residual stress that is termed as the differential thermal contraction stress. The final residual stress distribution is a result of a complex balance of stresses generated within the coating and substrate system. This distribution can be further analysed by attributing the stress state to several contributions under the formal framework proposed by Tsui & Clyne [46].

The overall stress state of the coating was modelled using neutron diffraction measurements to scan the residual stresses in the substrate (Fig. 7). These contributions are quantitatively presented in Table 4, where $\Delta\alpha$ is the difference in the CTE between the coating and substrate materials. Thermal mismatch stresses ($\Delta\varepsilon_{th}$) are attributed to differences in the thermal expansion coefficient (CTE) between the coating and substrate materials in conjunction with the temperature change after spraying; $\Delta\varepsilon_{th} = \Delta\alpha\Delta T$. CTE values for the SS316L substrate range from 10×10^{-6} to 17×10^{-6} K^{-1} between 273 and 373 K. The CTE values for Al_x-CoCrFeNi range from 8.84×10^{-6} to 11.25×10^{-6} K^{-1} between 423 and 1073 K and decreases monotonically with increasing Al content [58]. These CTE values for the coating and substrate materials are similar. Hence, the contribution of thermal mismatch stresses has been considered of minor influnce for the calculation of residual stress in this particular coating/substrate system, Table 4. The thermal contraction stresses were calculated from the temperature measurement data of the substrate that was logged during the coating deposition process. The elastic modulus of the PS AlCoCrFeNi coating (106 ± 7 GPa), obtained through microindentation was combined with the differential thermal expansion coefficient ($\Delta\alpha$) to calculate the thermal stress in coating due to cooling, Table 4.

Results of stress measurements for AlCoCrFeNi HEA coating on copper substrate shown in Fig. 7(a) and Table 4 indicate that the average residual stress in the coating is slightly tensile because the quenching stress dominates the thermal contraction stress. There is evidence of a compressive stress zone near the interface due to grit-blasting, which extends to less than 1 mm depth and is characterized by two fitting parameters.

In case of the copper substrate, both contributions to the overall stress, i.e., the quenching stress and thermal mismatch stress, are of similar magnitude but of the opposite sign, so their superposition results in a coating residual stress of a moderate magnitude. While quenching stress is relatively independent of the substrate material, although second order effects can be envisaged due to variation in thermal conductivities, the thermal mismatch stress is an effect of the first order and depends directly on the CTE differences between the coating and substrate. Therefore, if the substrate material is different, the thermal mismatch stress should be different. Thus, of a special interest is to determine the residual stresses in the system with the stainless steel substrate on the basis of experimental data obtained on the copper substrate system. These calculations are reported in Table 4, while recalculated residual stress profiles with respect to stainless steel substrate is plotted in Fig. 7(b).

As it seen that the change in substrate material results in a residual stress increase because (i) the contribution of the thermally generated stress changed significantly, while (ii) the quenching stress remained almost unchanged. In the new circumstances of the stainless steel substrate, the thermal mismatch stress does not balance the quenching stress anymore, but in fact, contributes more toward the tensile stress. The large tensile stresses are generally associated with preconditions of coating failure through cracking; hence the residual stresses pose a certain risk for the crack formation and propagation.

The stresses in AlCoCrFeNi HEA coatings discussed above are, in technical terms, macro-stresses. However, with the microstructural evidence (Fig. 2) that the material is multi-phase, yet another contribution to the total stress, so-called micro-stress should be present in a multiphase material such as the AlCoCrFeNi HEA coating. The micro-stresses must arise due to thermal mismatch between individual phases of the coating material, in a similar way as the thermal mismatch stress arises due to a CTE differences between the substrate and coating. However, these micro-stresses are physically scaled to the dimensions of a splat or less and they do not affect the results of the macro-stress analysis presented here. Additional fundamental research using high-energy synchrotron radiation could investigate such stresses.

3.5. *Scanning wear analysis*

As discussed earlier, the composite APS AlCoCrFeNi HEA coating can be categorized into three phases exhibiting distinct z-contrast and corresponding nanomechanical properties of nanohardness and reduced elastic modulus. A combination of these phases and properties governs the mechanical properties of the coating. The precise analysis of nanoscale wear behaviour of the individual phases would be valuable in assessing the overall tribological performance of the coating, both qualitatively and quantitatively. Essentially, the nanohardness and reduced elastic modulus

Table 4
Residual stress in APS AlCoCrFeNi HEA coating on 3.2 mm thick copper substrate determined from the experimental data and recalculated residual stress corresponding to the 3.0 mm thick SS316L substrate.

Substrate	Estimated deposition temperature of substrate (°C)	Differential thermal coefficient $\Delta\varepsilon = \Delta\alpha\Delta T$ μstrain	Quenching stress (MPa)	Average stress due to thermal mismatch (MPa)	Average stress due quenching (MPa)	Overall residual stress in coating (MPa)
Copper	184	−1150 ± 50	190 ± 45	−130	165	35
SS316L	184	~0	190	~0	170	170

obtained from nanoindentation experiments can be exploited further to qualitatively evaluate the wear resistance of the coating.

The ratio of nanohardness to reduced elastic modulus (H/E_r) signifies the material's ability to resist strain to failure. It is an appropriate parameter for assessing wear resistance at the nanoscale [59–61]. In addition, yield pressure measured as H^3/E_r^2, which characterizes the resistance to plastic deformation, can be employed to evaluate the nanoscale wear behaviour [60,62]. In the present study, the values of H and E_r measured at a load of 5000 μN were used to determine H/E_r and H^3/Er^2 for all three phases and are represented in Table 3. The black phase exhibited maximum wear resistance, followed by the grey and white phases, respectively.

The wear behaviour of the APS AlCoCrFeNi HEA coating was quantitatively assessed at nanoscale by conducting 2D scanning wear tests at four areas of the coating cross-section. Each area was scanned with three passes. Each pass included a combination of forward and reverse scans of whole area. The indenter tip was used to raster scan the chosen coating surface area of 10 μm × 10 μm with a specified normal force of 300 μN. The wear volume was calculated using the following formula:

$$|h_f| - |h_i| = \Delta h \tag{3}$$

$$A_w \times \Delta h = V_w \tag{4}$$

where, h_i is the average pre-scanning height of wear area (in nm), h_f is the average post-scanning height of wear area (in nm), Δh is the wear height (in nm), A_w is the wear scan area (in μm^2) and V_w is the final wear volume (in μm^3).

Table 5 summarises the wear volume of the four individual tested areas. The average wear volume of the APS AlCoCrFeNi coating was 0.92 ± 0.45 μm^3. Interactions between the indenter tip and coating phases occur at discrete asperities during the scanning wear test; hence, this test can recognise the wear behaviour of phases at local levels. In addition, the nano-wear mechanism can be applied to describe the overall coating wear behaviour. The wear performance of the black, grey and white phases can be investigated individually. Hence, the contour and line profiles of area 1 (A1) and area 4 (A4), which exhibited highest and lowest wear volume loss respectively, were investigated further.

Fig. 8 represents the contour and line profile analysis of area 1 (A1), wherein, Fig. 8(a) and (d) represent the pre- and post-scanning SEM images of worn area; Fig. 8(b) and (e) represent the pre- and post-scanning surface profile of the wear area examined using *in-situ* SPM integrated in the Triboindenter; and Fig. 8(c) and (f) represent the pre- and post-scanning contour profile of the wear area analysed using Origin Pro. In addition, to understand the wear behaviour of individual phases in terms of their topography (post-scanning depth), line profiling was analysed using Origin Pro; as shown in Fig. 8(g) and (h) as vertical and horizontal line profiles, respectively. Pink and blue vertical lines in Fig. 8(b) and (e) correspond to the pre- and post-scanning line profiles of the worn area and their depth is assessed in Fig. 8(g). Similarly, green and red horizontal lines in Fig. 8(b) and (e) correspond to the pre- and post-scanning line profile and depth is evaluated in Fig. 8(h). A similar pre- and post-processing procedure was applied to analyse the wear behaviour of area 4 (A4), Fig. 9.

As mentioned in Table 5, the wear volume of A4 was three times lower than that of A1. The main reason behind the large difference in wear volume for the two areas was the higher area coverage of the softer white phase (nanohardness = 5 GPa) within A1 (~67%) compared to A4 (~43%), as apparent in Fig. 8(a) and Fig. 9(a). The wear resistance of the white phase evaluated using H/E_r and H^3/Er^2 ratios was the lowest, Table 3. Hence, the material loss due to scanning wear would be highest for the white phase. This was verified using the contour and line profiling of the A1. The post-scanning contour profiling shown in Fig. 8(f) of A1 revealed that the white phase shows a significantly larger wear depth value compared to the grey and black phases. As represented in Fig. 8(g) and Fig. 8(**h**), the depth reduction of the white alloy phase was apparent in both vertical and horizontal line profiles. On the other hand, both grey and black oxide phases presented almost negligible material loss, since their wear depth was similar to the pre-scanning depth.

In addition, as seen in Fig. 8(d) and (e), a large pile-up wall was located at the edges of the scanning wear area. However, the pile-up along the area edges was concentrated in the white phase regions only. This indicated that pile-up mainly occurred due to wear of the white phase by the indenter tip. The significant height and thickness of pile-up specified that substantial plastic flow occurred during scanning wear. The white phase revealed the lowest H^3/Er^2 ratio, which signifies its endurance to severe plastic deformation. Furthermore, the pile-up of material was located mainly at the edge of the scan area; thereby implying that cutting wear was the prime wear mechanism rather than ploughing. The cutting mechanism operates when worn material is collected in front of the indenter after each line scan and transported, line-by-line, to the edge of the scan area [63].

Sample A4 exhibited behaviour dissimilar to A1, since the area percentages of the grey and black phases is higher than the white

Table 5
Scanning wear volume per area calculated using average height difference.

Area	Average pre-scanning height, h_i (nm)	Average post-scanning height, h_f (nm)	Wear height, Δh (nm)	Wear scan area, A_w (μm^2)	Wear volume, V_w (μm^3)
A1	0.12	- 14.40	14.28	100	1.43
A2	- 11.40	- 24.40	13	100	1.30
A3	7.10	1.68	5.42	100	0.54
A4	17	13	4	100	0.40

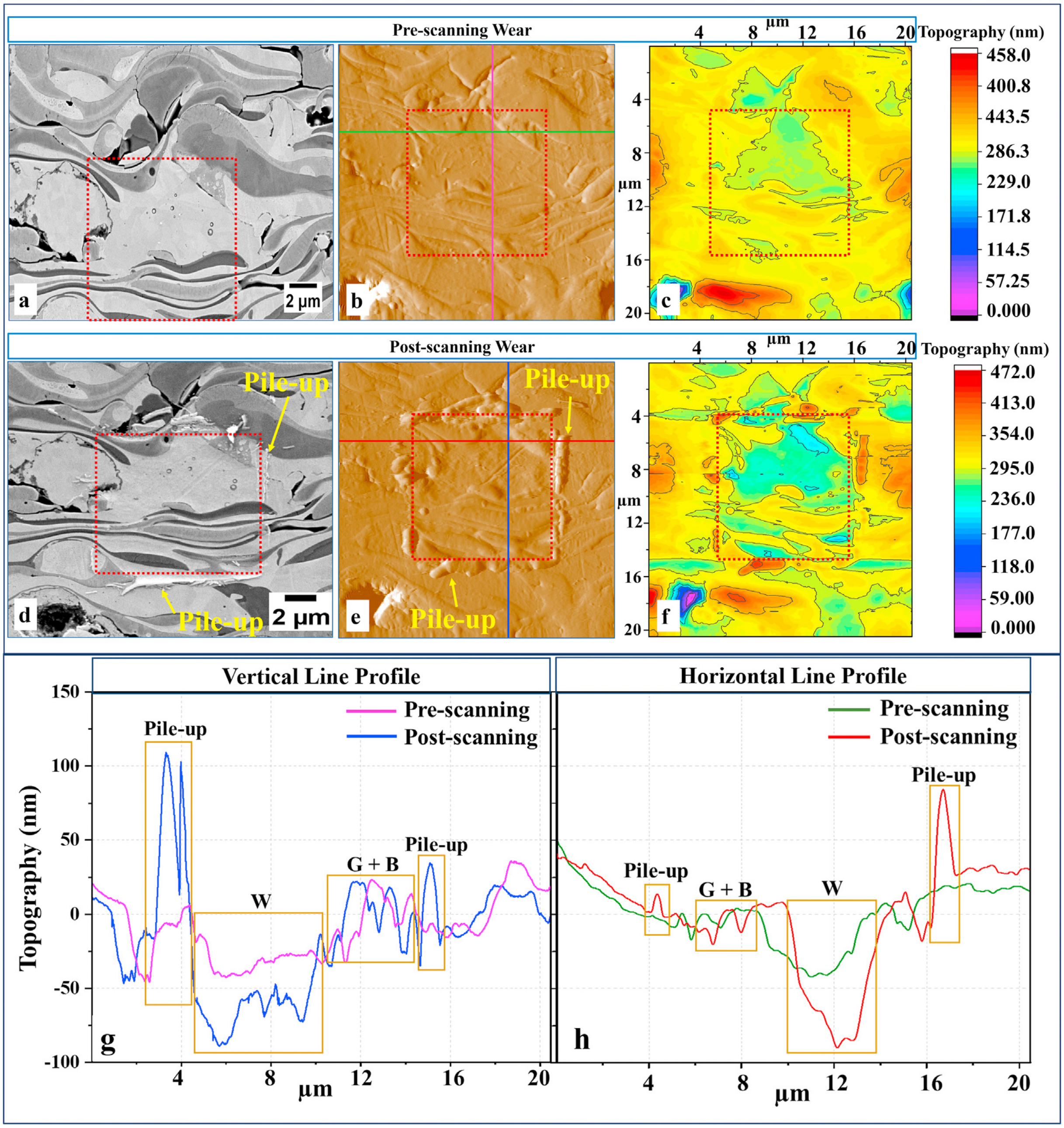

Fig. 8. (a) Cross-sectional SEM image showing distinct contrast phase area (A1) chosen for scanning wear testing, (b) *in-situ* scanning probe microscopy image prior to scanning wear, (c) contour map corresponding to pre-scanning *in-situ* scanning probe microscopy image, (d) post-scanning wear SEM image, (e) *in-situ* scanning probe microscopy image post-scanning wear, (f) contour map corresponding to post-scanning *in-situ* scanning probe microscopy image, (g) vertical line profiles corresponding to pink and blue line shown in (b) and (e), wherein top to bottom in (b) and (e) represents left to right line profile and, (h) horizontal line profiles corresponding to green and red line shown in (b) and (e) to show variation in wear depth within different phases and amount of pile-up across the worn area. (For interpretation of the references to colour in this figure legend, the reader is referred to the Web version of this article.)

phase (see Fig. 8(a) and Fig. 9(a)). Sample A4 exhibited the lowest wear volume loss. Moreover, the contour profiling (see Fig. 9(c) and (f)) of pre- and post-scanning wear revealed that wear depth was considerably smaller for the grey and whites phase compared to the white phase. Horizontal line profiling shown in Fig. 9(h) shows the difference between the three phases. The black phase endured almost no depth loss, while it was negligible for grey phase; hence corresponding to high wear resistance. The high wear resistance of both grey and black phase is well supported by their high nanohardness, H/E_r and H^3/Er^2 values. The pile-up wall seen in Fig. 9(d) and (e) occurred mainly due to wear of the white phase. The majority of pile-up was accumulated at the edge of the scan area; thus, the main wear mechanism was considered as cutting wear.

Scanning wear analysis of areas within PS AlCoCrFeNi coating shows that the wear performance of each phase within the coating is different. Both grey and black phase, which are predominately oxide phases created due to IFO, exhibited high wear resistance. This is evident from their low wear depth, owing to their high nanohardness and resistance to plastic deformation. Conversely, the multicomponent HEA phase (white) suffered significant plastic deformation and exhibited the lowest wear resistance. However, this difference between soft and hard phases would benefit in

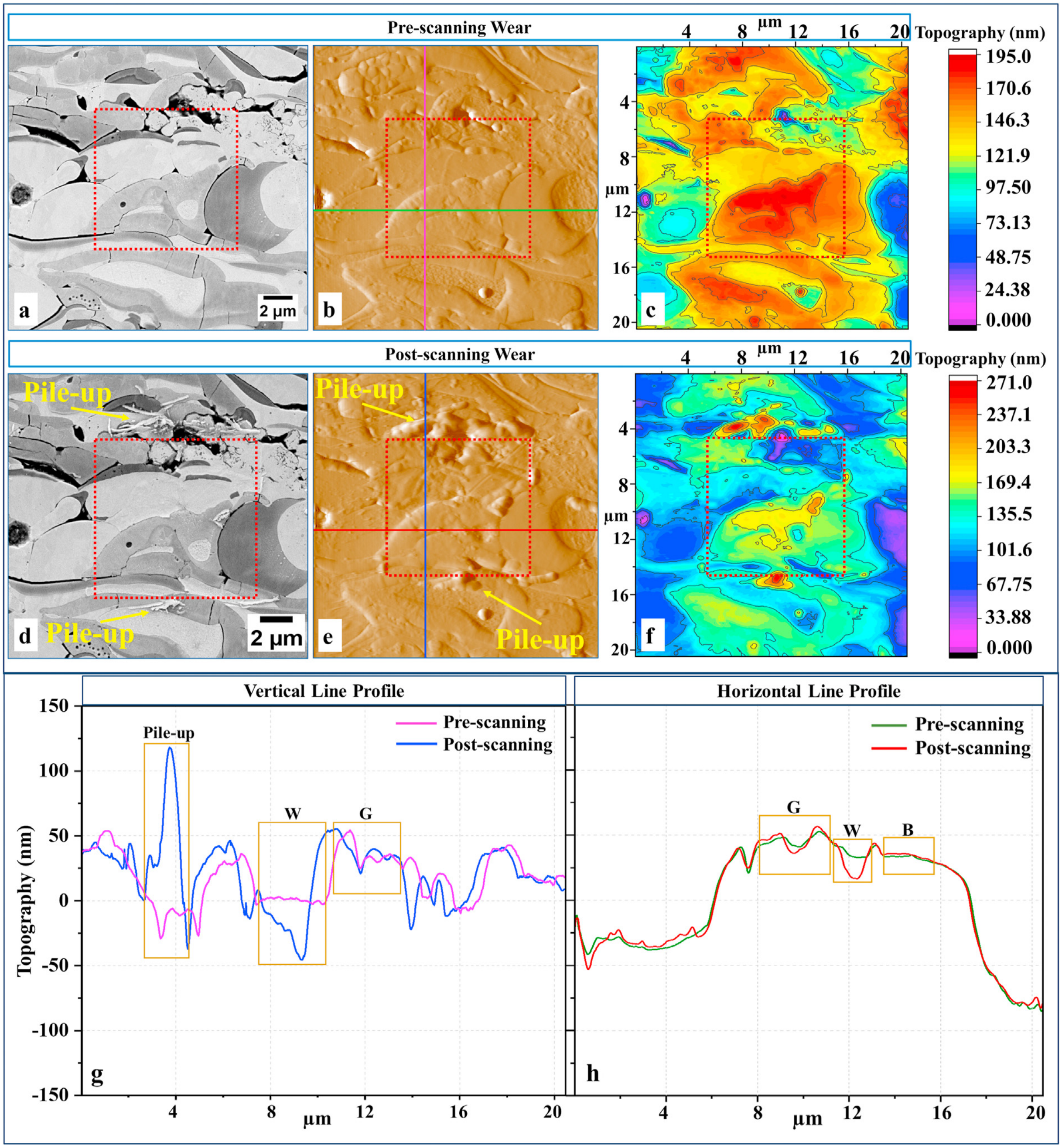

Fig. 9. (a) Cross-sectional SEM image showing distinct contrast phase area (A4) chosen for scanning wear testing, (b) *in-situ* scanning probe microscopy image prior to scanning wear, (c) contour map corresponding to pre-scanning *in-situ* scanning probe microscopy image, (d) post-scanning wear SEM image, (e) *in-situ* scanning probe microscopy image post-scanning wear, (f) contour map corresponding to post-scanning *in-situ* scanning probe microscopy image, (g) vertical line profiles corresponding to pink and blue line shown in (b) and (e), wherein top to bottom in (b) and (e) represents left to right line profile and, (h) horizontal line profiles corresponding to green and red line shown in (b) and (e) to show variation in wear depth within different phases and amount of pile-up across the worn area. (For interpretation of the references to colour in this figure legend, the reader is referred to the Web version of this article.)

balancing the overall wear performance of the coating. The precise evaluation of local wear behaviour of the different phases in the HEA coating provides us the opportunity to strategically design alloys with optimal wear characteristics.

3.6. Sliding wear behaviour

Room temperature and high temperature (HT = 500 °C) wear resistance of the plasma sprayed AlCoCrFeNi HEA coating was investigated against an Al_2O_3 ball as a counter body at a 10 N load over a sliding distance of 1000 m. The profile of the wear track was evaluated by 3D optical profilometry and is shown in Fig. 10(a) and Fig. 10(b). Fig. 10(c) represents the 2D depth and width profile of two tracks measured at the point shown by white arrow in Fig. 10(a) and (b). The 2D depth and width profiles evidenced that the wear track was deeper and wider at RT and, about 4 times deeper than that at HT. The diminution in depth and width of the wear track at HT indicates the high thermal stability, hot strength, and minimal plastic flow of the TS HEA coating. Joseph et al. [21] reported the high temperature wear performance of AlCoCrFeNi

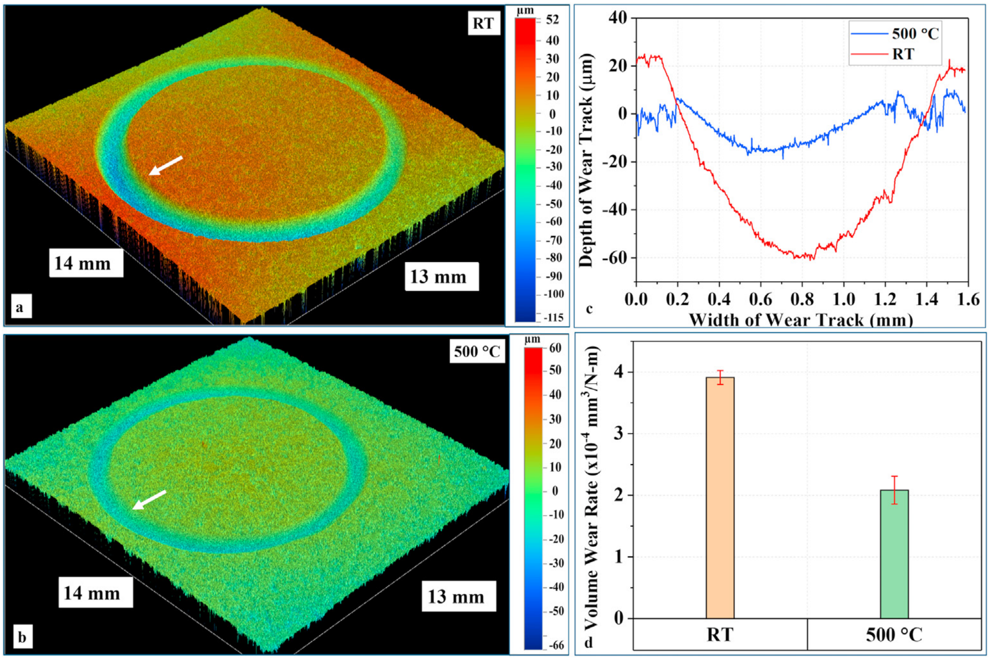

Fig. 10. Wear surface profilometry of (a) room temperature (RT) wear track, (b) high temperature wear track (500 °C), and (c) 2D wear depth profiles corresponds to bottom point of wear tracks as shown by white arrow and, (d) volume wear rate for APS AlCoCrFeNi coatings.

HEAs, with considerable decrease in width and depth of wear tracks with increasing temperature (RT, 300 °C, 600 °C and 900 °C); signifying good hot strength of AlCoCrFeNi HEAs.

The wear volume loss was calculated using laser confocal microscopy, which was further used to quantify the volume wear rate as per the Archard wear equation [64]. As illustrated in Fig. 10(d), the RT wear rate (3.91×10^{-4} mm^3/N-m) of plasma sprayed AlCoCrFeNi coating was approximately two times higher than the HT wear rate (2.08×10^{-4} mm^3/N-m). The friction coefficient values recorded were in the range of 0.86–0.92 and 0.39–0.46 for testing conducted at RT and HT, respectively. Hence, the outcome of wear testing postulated that plasma sprayed AlCoCrFeNi HEA coating exhibited superior wear resistance at HT (500 °C) as compared to RT.

The high values of friction coefficient (0.86–0.92) at RT indicated dominance of 2-body abrasion (sliding) between the HEA coating and counter body and, also represent the severity of wear. However, during HT testing, the coating sample was initially heated to 500 °C, and when temperature was stabilized, wear testing was carried out. An oxide layer could develop on the coating surface due to the increased test temperature. The oxide layer would act as a lubricant layer and prevent direct contact between two mating surfaces; thus, lowering the friction between two surfaces. The friction coefficient values obtained at HT (0.39–0.46) were almost half of the RT values and, also suggested operation of 3-body abrasion; i.e., rolling, between the two surfaces.

The morphologies of worn surfaces were inspected under SEM to understand the wear mechanisms and are illustrated in Fig. 11(a) and Fig. 11(b). The influence of increase in wear temperature was apparent from the disparity in the morphologies of the two worn surfaces. The RT wear surface morphology is shown in Fig. 11(a). The RT wear track (width = 1240 µm) of plasma sprayed AlCoCrFeNi coatings was rough and comprises a combination of surface wear modes and features. The harder Al_2O_3 ball (hardness = 19 GPa [65]) performed vigorous gliding action against a relatively softer plasma sprayed coating (hardness = 4 GPa), which led to severe inter-splat stepwise delamination wear of the coating, as shown in Fig. 11(a.1) and also supported by the high value of friction coefficient. As a consequence, delaminated pits of varying size can be observed at high magnification of the worn surface; suggesting surface fatigue. Moreover, as seen in Fig. 11(a), this delamination zone was limited to the central portion of the worn surface, indicating a difference in the local contact pressure of the Al_2O_3 ball and the coating surface. Nonetheless, the result was high volume loss of material.

In addition to the delamination wear, the RT wear surface can also be attributed to an adhesive wear mechanism. The adhesive wear surface appeared smoother and exhibited wear scratches and micro-cracks. Fig. 11(a.2) shows a wavy pattern comprising a sequence of parallel serrate ridges, in the form of a wavy pattern and perpendicular to the sliding direction, suggesting local severe adhesion between the counter body and coating.

The average chemical composition analysed by EDX of both worn and normal surfaces is presented in Fig. 12. The oxygen content of the worn surface was equivalent to that of the normal surface. The APS coatings possess inherent characteristics of high temperature in-flight oxidation (IFO). Hence it is hypothesized that the presence of oxygen in the worn surface arises from IFO and not frictional heat during wear. On this basis, the possibility of oxidative wear operating at RT has been excluded. In summary: RT wear mechanisms of plasma sprayed AlCoCrFeNi coating is an amalgamation of delamination wear and adhesive wear.

Tian et al. [66] inspected RT and high temperature wear behaviour of APS AlCoCrFeNiTi HEA coating and revealed that the coating experienced severe adhesive wear during RT wear testing, which is similar to our results. Surface morphology portrayed delamination of the splats and a protruding lip along the sliding direction. The splats constituting the lamellar microstructure of TS HEA coatings possess weak inter-splat bonding due to a limited 1/3rd interlamellar bonding ratio [67] and the presence of distinct phases with variable hardness. This would cause splats to pull away from the coating surface upon high contact pressure, instigating high volume loss. Furthermore, the plasma sprayed AlCoCrFeNi HEA coating comprises of composite microstructure of at least

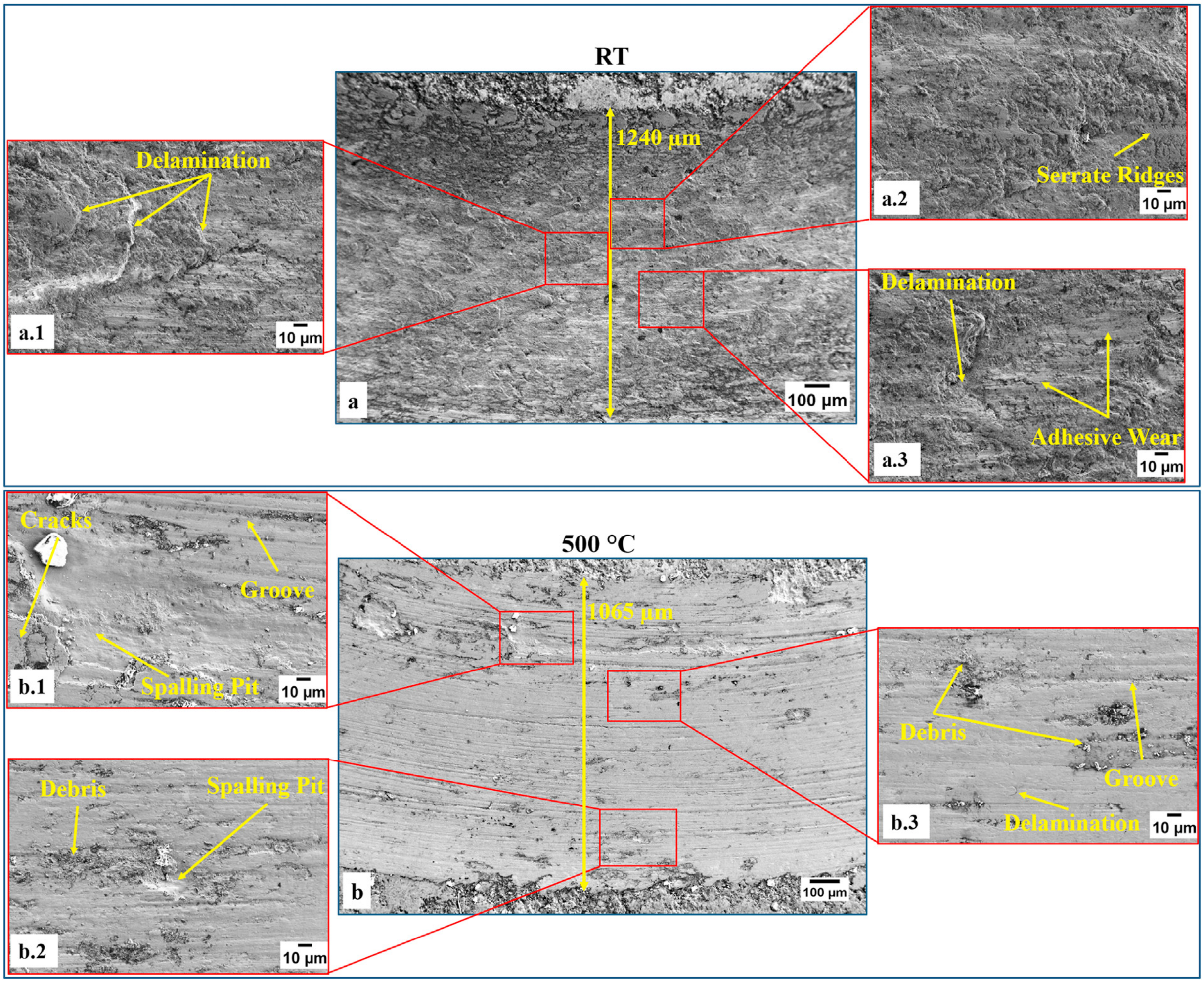

Fig. 11. (a) SEM micrograph of the worn surface of atmospheric plasma sprayed AlCoCrFeNi HEA coating after wear testing at room temperature. The corresponding high magnification images of red boxes drawn in (a) are shown in (a.1-a.3), respectively and; (b) SEM micrograph of the worn surface after wear testing at high temperature (500 °C). The corresponding high magnification images of red boxes drawn in (b) are shown in (b.1-b.3), respectively. (For interpretation of the references to colour in this figure legend, the reader is referred to the Web version of this article.)

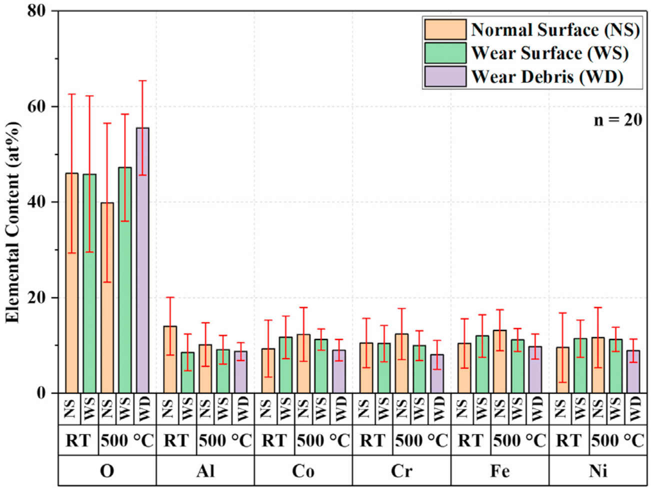

Fig. 12. Comparative analysis of average chemical composition of the room temperature and high temperature (500 °C) wear and normal surface, and wear debris obtained after high temperature wear testing.

three distinct phases in which all three phases exhibit different hardnesses. Locally, the nanowear behaviour of oxide phases was superior to that of the HEA phase within the coating. At the same time, higher hardness of oxides (black phase = 14 ± 8 GPa and grey phase = 12 ± 4 GPa) also renders them brittle compared to the metallic phase (white phase = 5 ± 2 GPa). The brittle nature would cause the oxides to fragment in the form of fine debris upon crack growth due to the high contact pressure of the counter body, which would then further contribute to the wear volume loss.

Fig. 11(b) shows the morphology of the worn surface tested at 500 °C (width = 1065 µm), which was distinctly different from the RT wear surface. The HT worn surface was relatively smooth and comprised of deep and shallow ploughing grooves parallel to the sliding direction, spalling pits, delamination, and evidence of fine wear debris; all of which signified 3-body abrasion between two surfaces. The observed worn surface features depicted oxidative and abrasive wear as the dominant wear mechanism. The high temperature worn surface also featured substantial plastic deformation along the grooves and at the edge of the wear track. The uniform distribution of parallel grooves indicated that the contact pressure of the Al_2O_3 ball was homogeneously distributed.

As presented in Fig. 12, the high percentage of oxygen on both the recovered wear debris and the worn surface suggested oxidative wear. The combinatorial effect of increase in test temperature and friction-induced heat due to repeated sliding leads to the development of a tribo-oxidation layer. This layer acts as a lubricating barrier between the HEA coating and the counter body, preventing direct coating-counter body contact, and reduces both the volume wear loss and friction coefficient values. As well, wear testing at high temperature can be regarded as sintering, which enhances the interlamellar bonding between the flattened splats. This would, boost the cohesion strength among splats, ultimately improving the coating's wear resistance [68].

EDS detected high oxygen contents in both the HT wear track and wear debris. Consequently, XPS analysis was performed on both the HT wear tack and normal HT coating surface to evaluate the elemental composition and chemical state of the oxide film, Fig. 13. A wide survey spectrum on the worn surface in Fig. 13(a) indicated the presence of a high intensity oxygen peak in addition to the peaks of aluminium, chromium, cobalt and iron. The wide spectrum survey of normal HT coating surface showed similar behaviour. XPS high resolution spectra shown in Fig. 13(b-e) confirmed the formation of an oxidation film comprising metal oxides such as Al_2O_3, Cr_2O_3, Fe_2O_3 and CoO and Co_3O_4; all developed due to the high temperature testing conditions and frictional heat. Likewise, Liu et al. [69] reported Al_2O_3, CoO, Cr_2O_3, Fe_2O_3, NiO and Fe_3O_4 oxides within wear scars during high temperature (600 °C) wear testing of laser clad AlCoCrFeNi coatings. The formation of this oxide layer diminishes the adhesion between two mating surfaces and combats the wear volume losses.

The importance of an oxide film for improving wear resistance can be judged by the differences in two wear rates, surface morphologies, and oxygen content within the worn surface and wear debris recovered from HT testing. The development of an oxide layer, which can act as a lubricating film, leads to an increase in wear resistance. In thermal sprayed HEA coatings, an oxide layer could form due to several mechanisms. First, the intrinsic IFO characteristics develop hard and brittle oxides within the coating that fragment as fine debris on crack growth. Second, the active metallic elements (such as Al, Cr, Fe) form oxides due to localized temperature rises from frictional heat and an elevated test temperature.

The difference in ability of PS AlCoCrFeNi HEA coating to resist wear at different temperatures is perceptible in this study. The HEA coating exhibited improved wear resistance at high temperature (500 °C) compared to RT. The HT wear testing led to development of an oxide layer, which acted as a solid lubricant between two surfaces; thus, influencing the wear behaviour profoundly. A transition of wear mechanism from severe delamination wear (2-body abrasion) at RT, to oxidative plus abrasive wear (3-body abrasion) at HT was observed in this study. The importance of *in-situ* oxide formation during HT wear testing to improve wear resistance has also been noted in studies on HEAs manufactured by different processes, such as atmospheric plasma sprayed AlCoCrFeNiTi [66], AlCoCrFeNiTi/Ni60 [70], FeCoNiCrMn [68]; HVOF sprayed $Al_{0.6}$TiCrFeCoNi [19]; melted and cast $Al_{0.25}$CoCrFeNi [20], CoCrFeMnNi and Al_xCoCrFeNi [21] and laser clad TiC reinforced AlCoCrFeNi [69].

In addition, both the RT and HT residual stress states play an important role in defining the wear behaviour of the current coating. As mentioned in Section 3.4, PS AlCoCrFeNi HEA coating on SS316L substrate is in tensile stress state (+170 MPa). Large tensile residual stresses, upon exceeding the fracture limit of the coating, would promote brittle cracking that leads to delamination under wear testing (as seen in Fig. 11(a)). These residual stresses thus adversely affect the coating wear behaviour at RT. Stewart et al. [71] and Liao et al. [72], in studies on the effect of residual stress on the abrasive wear behaviour of HVOF coating revealed that tensile residual stresses are detrimental to the wear resistance of the coating in the as-sprayed condition. However, wear testing at HT (500 °C) could anneal the coating sample and relieve stresses [73,74], which reduce the tensile residual stress state of as-sprayed coatings.

3.7. Electrochemical analysis

The corrosion behaviour of the plasma sprayed AlCoCrFeNi HEA coating was analysed using the potentiodynamic-polarization method in filtered sea water. The polarization curve demonstrates critical information such as corrosion potential (E_{corr}), current

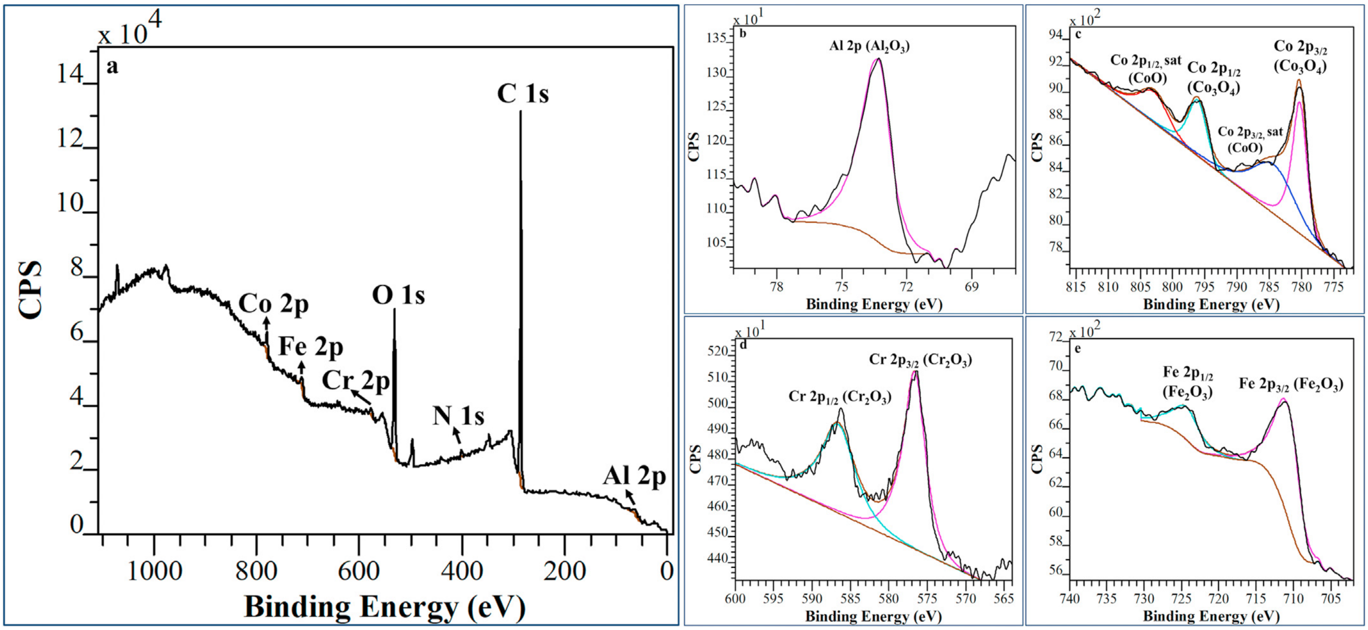

Fig. 13. XPS analysis of the wear track (500 °C) of plasma sprayed AlCoCrFeNi coating: (a) wide spectrum, (b) Al element, (c) Co element, (d) Cr element and, (e) Fe element.

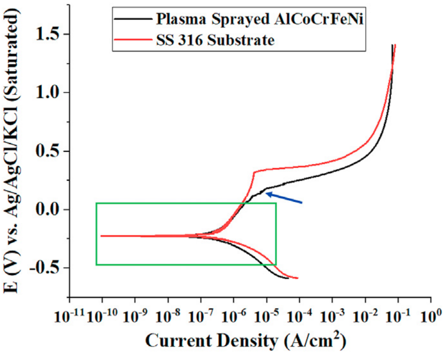

Fig. 14. Potentiodynamic polarization curves of both AlCoCrFeNi HEA coating and SS316L substrate with scan rate 1 mV/s in the sea water at room temperature. Green box represents the Tafel area and current fluctuation within HEA coating is shown by blue arrow. (For interpretation of the references to colour in this figure legend, the reader is referred to the Web version of this article.)

density (I_{corr}) and pitting potential (E_{pit}), which are important parameters for investigating the corrosion behaviour of a material. The polarization curves of the AlCoCrFeNi coating and SS316L substrate were measured at 1 mV/s scan rate in sea water at room temperature, Fig. 14. Neither the HEA coating, nor the substrate established an active to passive transition zone, and the curves transformed directly from the Tafel region to the passive region. This behaviour could be due to the high scan rate; however, this characteristic may also be attributed to the instantaneous formation of a protective film on the sample surface at the corrosion potential. Shi et al. [22,75] reported a similar polarization curve characteristic while analysing the electrochemical performance of cast $Al_xCoCrFeNi$ HEAs in 3.5 wt% NaCl solution.

The quantification of resistance to pitting/localized corrosion is given by the critical pitting potential (E_{pit}), which is the potential corresponding to a transition in the current density from steady to a rapid increment. Beyond E_{pit}, faster diffusion of Cl^- ions takes place on the coating surface through defects or corrosion prone phases and reduces the effect of the passivation film; resulting in localized corrosion. APS AlCoCrFeNi HEA coating exhibited a gradual increase in current density without any indication of a critical potential. However, current fluctuations were noticed in the HEA coating, shown by blue arrow in Fig. 14, which might be ascribed to the development and repassivation of metastable pits or selective corrosion [75,76]. On the contrary, a rapid increase in current density for SS316L substrate was observed, which represents the stabilization of pitting.

Table 6 compares the electrochemical data of the current HEA coating and substrate with HEAs manufactured by other techniques, as well as with several conventional alloys. PS AlCoCrFeNi HEA coating are observed to be more susceptible than SS316L substrate, not only to general corrosion, but also to localized corrosion. This increased susceptibility is indicated by their slightly higher I_{corr} and lowerE_{corr} values. However, the PS AlCoCrFeNi coating exhibited high resistance to general corrosion compared to plasma sprayed $(CoCrFeNi)_{95}Nb_5$ HEA coating [77], electrospark deposited AlCoCrFeNi [78], laser clad AlCoCrFeNi [79], AlCoCrFeNiSi [80], AlCoCrFeNiTi [79] and $Al_2CrFeCoCuTi$ [81] HEA coatings.

The surface morphology of the PS AlCoCrFeNi coating after the potentiodynamic polarization test were examined by SEM, Fig. 15. The coating surface appeared to be smooth. However, corrosive attack in the form of selective corrosion was observed, Fig. 15(a); although no preferential sites were detected for their incubation. High magnification SEM images further revealed variation in the size and shape of these selective corrosion spots. First, small bowl-shaped deep holes of ~5–10 μm size were observed, Fig. 15(b); and second, a large shallow region with numerous sub-micrometre sized holes was detected, Fig. 15(b) and (c). Wang et al. [77] analysed the corrosion behaviour of plasma sprayed $(CoCrFeNi)_{95}Nb_5$ in a 3.5 wt% NaCl solution and reported similar surface features after polarization testing.

Fig. 15(b) shows that the majority of multicomponent HEA phase (point 1) and oxide phase (point 3) regions were unaffected by corrosion attack since the local surface remained relatively flat and smooth. In addition, EDS analysis specified that their composition remained steady even after corrosion test. Point 2 refers to the area where micro-sized holes have been observed within the multicomponent HEA phase. This phenomenon may be attributed to the selective localized dissolution of aluminium, cobalt, nickel and iron in the form of oxides and hydroxides. This mechanism is implied because the region is rich in Cr (point 2), leaving the shallow corroded surface as a residual Cr-rich oxide, as seen in Fig. 15(b). The Cr-rich oxide may have behaved as a protective film and prevented severe corrosion, as evidenced by the fact that the micro-holes were superficial. In addition, a bulged product (point 4) with cracks was observed on the coating surface, exhibiting high oxygen and low metallic content. This feature could be associated to an oxide bubble, developed as a by-product, during the formation of a protective $Cr(OH)_3$ film on the coating surface [88].

The direct transition from a Tafel to a passive region suggested spontaneous formation of a protective film on the coating surface, which broke down on further increase in potential, as evident from the formation of localized corrosion sites on the coating surface. The corrosion resistance of the investigated HEA coating is postulated to originate from the development of an oxide film on the coating surface. This oxide film impedes the attack of electrolyte and reduces the dissolution of the corrosion prone phases [82]. The driving force for the development of corrosion resistant AlCoCrFeNi HEA based coatings lies in the ease of formation of a protective film that is based on alloying elements Al, Cr and Ni. Li et al. [78] evaluated the corrosion behaviour of electrospark deposited AlCoCrFeNi coating in 3.5 wt% NaCl. They reported improved corrosion resistance *vis-à-vis* the substrate AISI1045 steel and cast AlCoCrFeNi HEA, which was attributed to the formation of aluminium and chromium oxides on the HEA surface. Qiu et al. [23] investigated the electrochemical performance of cast $Al_xCoCrFeNiTi_y$, and described the development of Al_2O_3, Cr_2O_3, Fe_2O_3, Co_3O_4 and NiO on the corroded surface after the polarization test in 0.6 M NaCl. Similarly, formation of a largely Cr_2O_3 passivation film enhanced the corrosion resistance of plasma sprayed $(CoCrFeNi)_{95}Nb_5$ HEA coating [77].

However, with increased Al content in cast $Al_xCoCrFeNi$ HEA ($x = 0.3$, 0.5 and 0.7), a reduction in corrosion resistance was reported due to growth of a porous and thick aluminium oxide layer, which diminished the fraction of a more passive chromium oxide layer, resulting in deterioration of the alloys' corrosion resistance [75].

Applying similar concepts here, the plasma sprayed equi-atomic AlCoCrFeNi HEA coating exhibited inferior corrosion resistance than substrate SS316L, possibly due to the following reasons. First, the coating was composed of both aluminium and chromium. The standard potential of aluminium, at −1.66 V, is lower than −0.74 V for chromium [89]. Aluminium will, therefore, be more vulnerable to corrosion attack in sea water since it will preferentially act as an anode and expose the coating to selective corrosion. Second, the coating composition is equi-atomic AlCoCrFeNi HEA; i.e., the concentration of both aluminium and chromium are equal (~20–21 at %). Aluminium is more active than chromium; hence the probability of spontaneous growth of a thick and porous aluminium oxide layer [90] would be higher than for a passive chromium oxide

Table 6
The electrochemical data of (i) current atmospheric plasma sprayed AlCoCrFeNi HEA coating and substrate SS316L, (ii) HEAs manufactured by other techniques, and (iii) several conventional alloys.

Material	Process	Solution	Ecorr (mV_{SCE})	Icorr ($\mu A/cm^2$)	Epit (mV_{SCE})	Reference
AlCoCrFeNi	Atmospheric plasma spray	Sea water	- 321	0.83	–	Current study
$(CoCrFeNi)_{95}Nb_5$	Atmospheric plasma spray	3.5 wt% NaCl	- 370	7.23	260	[77]
AlCoCrFeNi	Laser cladding	3.5 wt% NaCl	- 427.8	2.50	–	[79]
AlCoCrFeNi	Laser cladding	3.5 wt% NaCl	- 270	0.07	- 208	[82]
FeCoCrAlNi	Laser surface alloying	3.5 wt% NaCl	- 167	0.07	257	[83]
AlCoCrFeNi	Direct laser fabrication	0.6 M NaCl	- 264.1	0.12	5.1	[84]
AlCoCrFeNi	Electrospark deposition	3.5 wt% NaCl	- 349	0.01	–	[78]
AlCoCrFeNi	Cast	3.5 wt% NaCl	- 294	0.09	–	[78]
$Al_{0.9}CoCrFeNi$	Cast	0.6 M NaCl	- 252	0.24	290	[23]
AlCoCrFeNiTi	Laser cladding	3.5 wt% NaCl	- 467.4	2.16	–	[79]
AlCoCrFeNiSi	Laser cladding	3.5 wt% NaCl	- 326	0.65	–	[80]
$Al_2CrFeCoCuTi$	Laser cladding	3.5 wt% NaCl	- 510	68	–	[81]
$Al_2CrFeCoCuTiNi$	Laser cladding	3.5 wt% NaCl	- 220	13	–	[81]
CrMnFeCoNi	Laser surface alloying	3.5 wt% NaCl	- 99.5	0.11	218	[85]
CoCrFeNi	Cast	0.6 M NaCl	- 248	0.11	442	[23]
SS316L	–	Sea water	- 274	0.26	274	Current study
AISI 304		3.5 wt% NaCl	- 482	7	–	[80]
AA1100	–	Sea water	- 920	–	- 575	[86]
AA5083	–	Sea water	- 950	–	- 680	[86]
γ - TiAl	–	Sea water	- 672	8.24	–	[87]
γ - TiAl	–	3.5 wt% NaCl	- 428	1.94	–	[87]

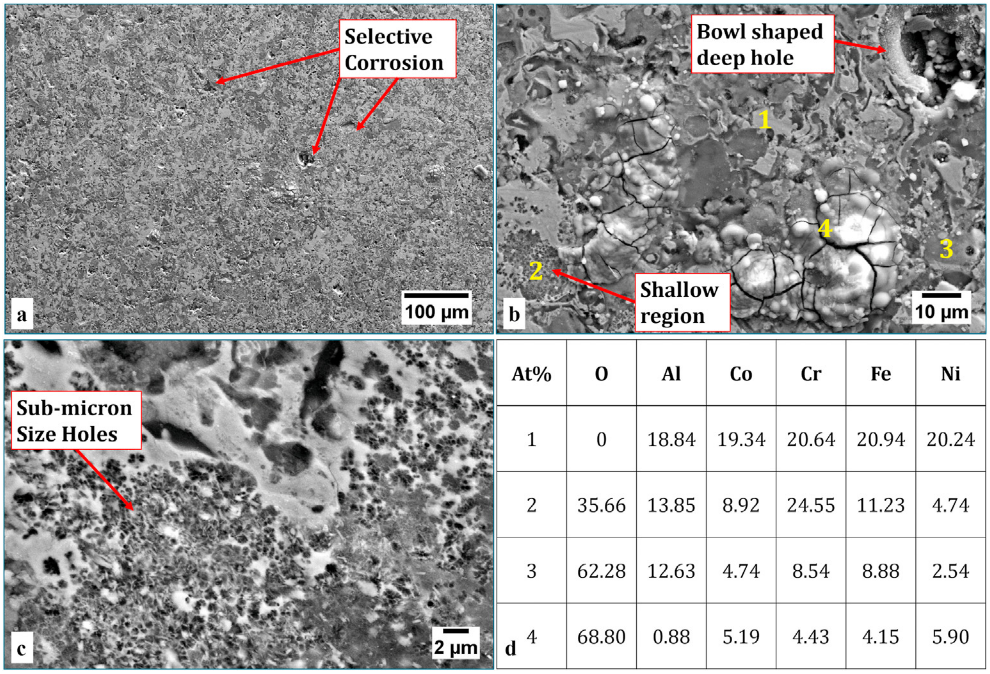

At%	O	Al	Co	Cr	Fe	Ni
1	0	18.84	19.34	20.64	20.94	20.24
2	35.66	13.85	8.92	24.55	11.23	4.74
3	62.28	12.63	4.74	8.54	8.88	2.54
4	68.80	0.88	5.19	4.43	4.15	5.90

Fig. 15. (a) Surface morphology of the AlCoCrFeNi coating surface after potentiodynamic polarization tests, (b) high magnification SEM images of coating surface representing formation of pits and bulged oxide product, (c) micro-pits observed on coating surface and, (d) EDS analysis corresponding to the points mentioned in (b).

layer.

The existence of inherent microstructural inhomogeneities within the PS AlCoCrFeNi coating could lead to inferior corrosion resistance. HEA coatings produced through plasma spray develop a lamellar microstructure, which include formation of porosity due to incomplete intersplat bonding; multi-phase formation; unmelts; and thermal and contraction stresses. The presence of porosity in a thermal spray coating substantially influences its electrochemical performance, mostly in a destructive manner [91–94]. Also, the HEA feedstock transformed to a multi-phase coating after plasma spray process. This includes development of oxides due to IFO. The internal chemistry of these oxides would affect the uniformity of the passivation film; thereby influencing the corrosion behaviour of the coating in terms of micro-galvanic corrosion.

The combinatorial effects described above negatively impact the corrosion resistance of PS AlCoCrFeNi HEA coating. In contrast, the substrate SS316L is composed of 16–18 wt% chromium and 10–14 wt% nickel. The high chromium content would lay the foundation for the development of a passive and compact Cr_2O_3 layer that is well-supported by the formation of a NiO layer [95]; which leads to superior corrosion resistance. Another fact is that the electrochemical data; i.e., E_{corr} and I_{corr} for the HEA coating, exhibits only slightly lower resistance to general and localized corrosion compared to the SS316L in sea water. The identical anodic and cathodic polarization behaviour of the HEA coating to SS316L indicates that the AlCoCrFeNi-based HEAs have strong potential as corrosion resistant materials.

4. Conclusions

The conclusions of this study are:

a) Plasma sprayed equi-atomic AlCoCrFeNi HEA coatings are composed of a lamellar microstructure constituted by a mixture of three types of phases exhibiting distinct z-contrast; (i) a black (B) phase that is an Al-rich oxide phase, (ii) a grey (G) phase that is an Al—Cr—Fe rich oxide, and (iii) a white (W) phase that is an Al-depleted multicomponent HEA phase.
b) The ultra-high speed nanoindentation XPM technique was used for evaluating the localized hardness and reduced elastic modulus, in combination with *in-situ* scanning probe microscopy and scanning electron microscopy.
c) Statistical analysis of observed nanoindentation datasets revealed that the black phase exhibited the highest hardness and the white phase lowest. Also, pile-up around the white phase indicated that the alloy phase endured extensive localized plastic deformation. Moreover, Weibull regression analysis showed that hardness within the black phase is least homogenous compared to the other two phases. However, the reduced elastic modulus displayed only a minor difference among the phases.
d) Superimposing the concepts of statistical analysis and nanoindentation XPM mapping has been shown to be a powerful tool to establish relationships between local mechanical properties and multi-phase microstructures. This technique can also be exploited to evaluate the influence of interphase, neighbouring cracks and inter/intra splat behaviour, to understand the overall performance of coatings.
e) Residual stress in a plasma sprayed AlCoCrFeNi HEA coating is tensile since the quenching stress mechanism dominates over that of thermally generated stress from thermal expansion mismatches between the coating and substrate materials.
f) In nano-scale scanning wear test, the coating cross-sectional area with a higher fraction of the softer white phase exhibited a high wear volume loss and vice versa. The wear resistance of grey and black oxide phases generated by in-flight oxidation (IFO) was superior to that of the multicomponent HEA phase (white), as evident by their substantial differences in wear depth. Concurrently, white phase with the lowest nanohardness suffered significant plastic deformation, as evident from pile-up around edges of the worn area; implying that cutting wear was the dominant wear mechanism operating at nanoscale.
g) Plasma sprayed AlCoCrFeNi HEA coatings exhibited superior wear resistance at high temperature (500 °C) than at room temperature. A two-fold decrease in volume wear was observed. The wear mechanism changes from a combination of delamination wear and adhesive wear at room temperature, to oxidative and abrasive wear at elevated temperature.
h) Potentiodynamic polarization tests show that plasma sprayed AlCoCrFeNi HEA coatings displayed slightly lower corrosion resistance than SS316L substrate, in both general and localized corrosion. However, identical polarization curve characteristics indicated that AlCoCrFeNi-based HEAs are promising corrosion resistant materials.

CRediT authorship contribution statement

Ashok Meghwal: Conceptualization, Methodology, Validation, Formal analysis, Investigation, Writing - original draft, Visualization. **Ameey Anupam:** Methodology, Investigation, Writing - original draft, Visualization. **Vladimir Luzin:** Validation, Formal analysis, Investigation, Writing - original draft, Visualization. **Christiane Schulz:** Validation, Investigation, Writing - review & editing. **Colin Hall:** Validation, Investigation, Writing - review & editing. **B.S. Murty:** Writing - review & editing. **Ravi Sankar Kottada:** Writing - review & editing. **Christopher C. Berndt:** Conceptualization, Writing - review & editing, Visualization, Supervision, Funding acquisition. **Andrew Siao Ming Ang:** Conceptualization, Methodology, Investigation, Writing - review & editing, Visualization, Supervision, Funding acquisition.

Declaration of competing interest

The authors declare that they have no known competing financial interests or personal relationships that could have appeared to influence the work reported in this paper.

Acknowledgement

This work is supported under a Swinburne University Postgraduate Research Award (SUPRA). We thank Coherent Scientific and Bruker for offering an extended demonstration period of their nanoindentation XPM technology at Swinburne University of Technology. This study was also supported by the Australian Research Council (ARC) under the Industrial Transformation Training Centre project IC180100005 that is titled “Surface Engineering for Advanced Materials”, SEAM. The neutron diffraction experimental work was supported through the ANSTO user access programme (proposal P3925). We are grateful for the additional support for the industrial, university and other organization partners who have contributed to the establishment and support of SEAM. The authors acknowledge the facilities, scientific and technical assistance of Microscopy Australia at the University of South Australia, a facility that is funded by the University of South Australia, the State and Federal Governments. This work was performed in part at the South Australian node of the Australian National Fabrication Facility under the National Collaborative Research Infrastructure Strategy.

References

[1] J.-W. Yeh, S.-K. Chen, S.-J. Lin, J.-Y. Gan, T.-S. Chin, T.-T. Shun, C.-H. Tsau, S.-Y. Chang, Nanostructured high-entropy alloys with multiple principal elements: novel alloy design concepts and outcomes, Adv. Eng. Mater. 6 (5) (2004) 299—303.
[2] B. Cantor, I.T.H. Chang, P. Knight, A.J.B. Vincent, Microstructural development in equiatomic multicomponent alloys, Mater. Sci. Eng., A 375—377 (1—2) (2004) 213—218.
[3] Y. Zhang, T.T. Zuo, Z. Tang, M.C. Gao, K.A. Dahmen, P.K. Liaw, Z.P. Lu, Microstructures and properties of high-entropy alloys, Prog. Mater. Sci. 61 (2014) 1—93.
[4] B.S. Murty, J.W. Yeh, S. Ranganathan, P.P. Bhattacharjee, High-Entropy Alloys, 2^{nd}, Elsevier, 2019, p. 388, 19 March 2019.
[5] D.B. Miracle, O.N. Senkov, A critical review of high entropy alloys and related concepts, Acta Mater. 122 (2017) 448—511.
[6] S. Varalakshmi, M. Kamaraj, B.S. Murty, Synthesis and characterization of nanocrystalline AlFeTiCrZnCu high entropy solid solution by mechanical alloying, J. Alloys Compd. 460 (1—2) (2008) 253—257.
[7] W.-R. Wang, W.-L. Wang, S.-C. Wang, Y.-C. Tsai, C.-H. Lai, J.-W. Yeh, Effects of Al addition on the microstructure and mechanical property of $Al_xCoCrFeNi$ high-entropy alloys, Intermetallics 26 (2012) 44—51.
[8] B. Schuh, F. Mendez-Martin, B. Völker, E.P. George, H. Clemens, R. Pippan, A. Hohenwarter, Mechanical properties, microstructure and thermal stability of a nanocrystalline CoCrFeMnNi high-entropy alloy after severe plastic deformation, Acta Mater. 96 (2015) 258—268.

[9] X.B. Feng, W. Fu, J.Y. Zhang, J.T. Zhao, J. Li, K. Wu, G. Liu, J. Sun, Effects of nanotwins on the mechanical properties of $Al_xCoCrFeNi$ high entropy alloy thin films, Scripta Mater. 139 (2017) 71–76.

[10] T.M. Butler, M.L. Weaver, Oxidation behavior of arc melted AlCoCrFeNi multi-component high-entropy alloys, J. Alloys Compd. 674 (2016) 229–244.

[11] A. Munitz, S. Salhov, S. Hayun, N. Frage, Heat treatment impacts the micro-structure and mechanical properties of AlCoCrFeNi high entropy alloy, J. Alloys Compd. 683 (2016) 221–230.

[12] S. Praveen, A. Anupam, R. Tilak, R.S. Kottada, Phase evolution and thermal stability of AlCoCrFe high entropy alloy with carbon as unsolicited addition from milling media, Mater. Chem. Phys. 210 (2018) 57–61.

[13] K.B. Zhang, Z.Y. Fu, J.Y. Zhang, W.M. Wang, H. Wang, Y.C. Wang, Q.J. Zhang, J. Shi, Microstructure and mechanical properties of $CoCrFeNiTiAl_x$ high-entropy alloys, Mater. Sci. Eng., A 508 (1) (2009) 214–219.

[14] B. Gwalani, S. Gorsse, D. Choudhuri, Y. Zheng, R.S. Mishra, R. Banerjee, Tensile yield strength of a single bulk $Al_{0.3}CoCrFeNi$ high entropy alloy can be tuned from 160 MPa to 1800 MPa, Scripta Mater. 162 (2019) 18–23.

[15] J.W. Qiao, S.G. Ma, E.W. Huang, C.P. Chuang, P.K. Liaw, Y. Zhang, Microstructural characteristics and mechanical behaviors of AlCoCrFeNi high-entropy alloys at ambient and cryogenic temperatures, Mater. Sci. Forum 688 (2011) 419–425.

[16] B. Gludovatz, A. Hohenwarter, K.V.S. Thurston, H. Bei, Z. Wu, E.P. George, R.O. Ritchie, Exceptional damage-tolerance of a medium-entropy alloy CrCoNi at cryogenic temperatures, Nat. Commun. 7 (2016).

[17] D. Li, C. Li, T. Feng, Y. Zhang, G. Sha, J.J. Lewandowski, P.K. Liaw, Y. Zhang, High-entropy $Al_{0.3}CoCrFeNi$ alloy fibers with high tensile strength and ductility at ambient and cryogenic temperatures, Acta Mater. 123 (2017) 285–294.

[18] P.F. Zhou, D.H. Xiao, T.C. Yuan, Microstructure, mechanical and corrosion properties of AlCoCrFeNi high-entropy alloy prepared by spark plasma sintering, Acta Metall. Sin. (Engl. Lett.) 33 (7) (2020) 937–946.

[19] L. Chen, K. Bobzin, Z. Zhou, L. Zhao, M. Öte, T. Königstein, Z. Tan, D. He, Wear behavior of HVOF-sprayed $Al_{0.6}TiCrFeCoNi$ high entropy alloy coatings at different temperatures, Surf. Coating. Technol. 358 (2019) 215–222.

[20] L.M. Du, L.W. Lan, S. Zhu, H.J. Yang, X.H. Shi, P.K. Liaw, J.W. Qiao, Effects of temperature on the tribological behavior of $Al_{0.25}CoCrFeNi$ high-entropy alloy, J. Mater. Sci. Technol. 35 (5) (2019) 917–925.

[21] J. Joseph, N. Haghdadi, K. Shamlaye, P. Hodgson, M. Barnett, D. Fabijanic, The sliding wear behaviour of CoCrFeMnNi and $Al_xCoCrFeNi$ high entropy alloys at elevated temperatures, Wear 428–429 (2019) 32–44.

[22] Y. Shi, L. Collins, R. Feng, C. Zhang, N. Balke, P.K. Liaw, B. Yang, Homogenization of $Al_xCoCrFeNi$ high-entropy alloys with improved corrosion resistance, Corrosion Sci. 133 (2018) 120–131.

[23] Y. Qiu, S. Thomas, D. Fabijanic, A.J. Barlow, H.L. Fraser, N. Birbilis, Microstructural evolution, electrochemical and corrosion properties of $Al_xCoCrFeNiTi_y$ high entropy alloys, Mater. Des. 170 (2019) 107698.

[24] L. Wang, D. Mercier, S. Zanna, A. Seyeux, M. Laurent-Brocq, L. Perrière, I. Guillot, P. Marcus, Study of the surface oxides and corrosion behaviour of an equiatomic CoCrFeMnNi high entropy alloy by XPS and ToF-SIMS, Corrosion Sci. 167 (2020) 108507.

[25] P. Li, A. Wang, C.T. Liu, A ductile high entropy alloy with attractive magnetic properties, J. Alloys Compd. 694 (2017) 55–60.

[26] A. Meghwal, A. Anupam, B.S. Murty, C.C. Berndt, R.S. Kottada, A.S.M. Ang, Thermal spray high-entropy alloy coatings: a review, J. Therm. Spray Technol. 29 (5) (2020) 857–893.

[27] A.S.M. Ang, C.C. Berndt, M.L. Sesso, A. Anupam, S. Praveen, R.S. Kottada, B.S. Murty, Plasma-sprayed high entropy alloys: microstructure and properties of AlCoCrFeNi and MnCoCrFeNi, Metall. Mater. Trans. A-Phys. Metall. Mater. Sci. 46A (2) (2015) 791–800.

[28] D.Y. Lin, N.N. Zhang, B. He, B.Q. Jin, Y. Zhang, D.Y. Li, F.Y. Dong, Influence of laser re-melting and vacuum heat treatment on plasma-sprayed FeCoCrNiAl alloy coatings, J. Iron Steel Res. Int. 24 (12) (2017) 1199–1205.

[29] K.C. Cheng, J.H. Chen, S. Stadler, S.H. Chen, Properties of atomized AlCoCrFeNi high-entropy alloy powders and their phase-adjustable coatings prepared via plasma spray process, Appl. Surf. Sci. 478 (2019) 478–486.

[30] A. Anupam, R.S. Kottada, S. Kashyap, A. Meghwal, B.S. Murty, C.C. Berndt, A.S.M. Ang, Understanding the microstructural evolution of high entropy alloy coatings manufactured by atmospheric plasma spray processing, Appl. Surf. Sci. 505 (2020) 144117.

[31] M. Srivastava, M. Jadhav, Chethan, R.P.S. Chakradhar, M. Muniprakash, S. Singh, Synthesis and properties of high velocity oxy-fuel sprayed $FeCoCrNi_2Al$ high entropy alloy coating, Surf. Coating. Technol. 378 (2019) 124950.

[32] A. Anupam, S. Kumar, N.M. Chavan, B.S. Murty, R.S. Kottada, First report on cold-sprayed AlCoCrFeNi high-entropy alloy and its isothermal oxidation, J. Mater. Res. 34 (5) (2019) 796–806.

[33] A.C. Fischer-Cripps, Critical review of analysis and interpretation of nanoindentation test data, Surf. Coating. Technol. 200 (14) (2006) 4153–4165.

[34] V. Luzin, A. Valarezo, S. Sampath, Through-thickness residual stress measurement in metal and ceramic spray coatings by neutron diffraction, Mater. Sci. Forum 571–572 (2008) 315–320.

[35] A.S.M. Ang, C.C. Berndt, A review of testing methods for thermal spray coatings, Int. Mater. Rev. 59 (4) (2014) 179–223.

[36] Astm E1920-03, Standard Guide for Metallographic Preparation of Thermal Sprayed Coatings, ASTM International, West Conshohocken, PA, 2014, 2014.

[37] W.C. Oliver, G.M. Pharr, Measurement of hardness and elastic modulus by instrumented indentation: advances in understanding and refinements to methodology, J. Mater. Res. 19 (1) (2004) 3–20.

[38] A.C. Fischer-Cripps, Review of analysis methods for sub-micron indentation testing, Vacuum 58 (4) (2000) 569–585.

[39] E. Broitman, Indentation hardness measurements at macro-, micro-, and nanoscale: a critical overview, Tribol. Lett. 65 (23) (2017).

[40] O. Kirstein, V. Luzin, U. Garbe, The strain-scanning diffractometer kowari, Neutron News 20 (4) (2009) 34–36.

[41] V. Luzin, A. Vackel, A. Valarezo, S. Sampath, Neutron through-thickness stress measurements in coatings with high spatial resolution, Mater. Sci. Forum 905 (2017) 165–173.

[42] V. Luzin, K. Spencer, M. Zhang, N. Matthews, J. Davis, M. Saleh, Residual stresses in cold spray coatings, in: Cold-spray Coatings: Recent Trends and Future Perspectives, 1st, Springer International Publishing, 2018, pp. 451–480.

[43] I.C. Noyan, J.B. Cohen, Residual Stress: Measurement by Diffraction and Interpretation, first ed., Springer-Verlag New York, 1987, p. 276.

[44] T. Gnaupel-Herold, ISODEC: software for calculating diffraction elastic constants, J. Appl. Crystallogr. 45 (3) (2012) 573–574.

[45] A.M. Venter, V. Luzin, O.P. Oladijo, L.A. Cornish, N. Sacks, Study of interactive stresses in thin WC-Co coating of thick mild steel substrate using high-precision neutron diffraction, Mater. Sci. Forum 772 (2014) 161–165.

[46] Y.C. Tsui, T.W. Clyne, An analytical model for predicting residual stresses in progressively deposited coatings Part 1: planar geometry, Thin Solid Films 306 (1) (1997) 23–33.

[47] W. Ji, Z. Fu, W. Wang, H. Wang, J. Zhang, Y. Wang, F. Zhang, Mechanical alloying synthesis and spark plasma sintering consolidation of CoCrFeNiAl high-entropy alloy, J. Alloys Compd. 589 (2014) 61–66.

[48] M. Vaidya, A. Prasad, A. Parakh, B.S. Murty, Influence of sequence of elemental addition on phase evolution in nanocrystalline AlCoCrFeNi: novel approach to alloy synthesis using mechanical alloying, Mater. Des. 126 (2017) 37–46.

[49] A. Manzoni, H. Daoud, R. Völkl, U. Glatzel, N. Wanderka, Phase separation in equiatomic AlCoCrFeNi high-entropy alloy, Ultramicroscopy 132 (2013) 212–215.

[50] Y.V. Milman, A.A. Golubenko, S.N. Dub, Indentation size effect in nanohardness, Acta Mater. 59 (20) (2011) 7480–7487.

[51] Z.M. Jiao, M.Y. Chu, H.J. Yang, Z.H. Wang, J.W. Qiao, Nanoindentation characterised plastic deformation of a $Al_{0.5}CoCrFeNi$ high entropy alloy, Mater. Sci. Technol. 31 (10) (2015) 1244–1249.

[52] G. Muthupandi, K.R. Lim, Y.-S. Na, J. Park, D. Lee, H. Kim, S. Park, Y.S. Choi, Pile-up and sink-in nanoindentation behaviors in AlCoCrFeNi multi-phase high entropy alloy, Mater. Sci. Eng., A 696 (2017) 146–154.

[53] C.K. Lin, C.C. Berndt, Statistical analysis of microhardness variations in thermal spray coatings, J. Mater. Sci. 30 (1) (1995) 111–117.

[54] S. Praveen, B.S. Murty, R.S. Kottada, Phase evolution and densification behavior of nanocrystalline multicomponent high entropy alloys during spark plasma sintering, J. Occup. Med. 65 (12) (2013) 1797–1804.

[55] D. Goldbaum, R.R. Chromik, S. Yue, E. Irissou, J.G. Legoux, Mechanical property mapping of cold sprayed Ti splats and coatings, J. Therm. Spray Technol. 20 (3) (2011) 486–496.

[56] P. Suresh Babu, P. Chanikya Rao, A. Jyothirmayi, P. Sudharshan Phani, L. Rama Krishna, D. Srinivasa Rao, Evaluation of microstructure, property and performance of detonation sprayed $WC-(W,Cr)_2C-Ni$ coatings, Surf. Coating. Technol. 335 (2018) 345–354.

[57] P. Sudharshan Phani, W.C. Oliver, A critical assessment of the effect of indentation spacing on the measurement of hardness and modulus using instrumented indentation testing, Mater. Des. 164 (2019) 107563.

[58] H.-P. Chou, Y.-S. Chang, S.-K. Chen, J.-W. Yeh, Microstructure, thermophysical and electrical properties in $Al_xCoCrFeNi$ ($0 \leq x \leq 2$) high-entropy alloys, Mater. Sci. Eng., B 163 (3) (2009) 184–189.

[59] A. Leyland, A. Matthews, On the significance of the H/E ratio in wear control: a nanocomposite coating approach to optimised tribological behaviour, Wear 246 (1) (2000) 1–11.

[60] H. Attar, S. Ehtemam-Haghighi, D. Kent, I.V. Okulov, H. Wendrock, M. Bönisch, A.S. Volegov, M. Calin, J. Eckert, M.S. Dargusch, Nanoindentation and wear properties of Ti and Ti-TiB composite materials produced by selective laser melting, Mater. Sci. Eng., A 688 (2017) 20–26.

[61] L.J. Zhang, Z.K. Jiang, M.D. Zhang, J.T. Fan, D.J. Liu, P.F. Yu, G. Li, R.P. Liu, Effect of solid carburization on the surface microstructure and mechanical properties of the equiatomic CoCrFeNi high-entropy alloy, J. Alloys Compd. 769 (2018) 27–36.

[62] J. Musil, F. Kunc, H. Zeman, H. Poláková, Relationships between hardness, Young's modulus and elastic recovery in hard nanocomposite coatings, Surf. Coating. Technol. 154 (2) (2002) 304–313.

[63] K.I. Schiffmann, Microtribological/mechanical testing in 0, 1 and 2 dimensions: a comparative study on different materials, Wear 265 (11–12) (2008) 1826–1836.

[64] J.F. Archard, Contact and rubbing of flat surfaces, J. Appl. Phys. 24 (8) (1953) 981–988.

[65] G. Bolelli, V. Cannillo, L. Lusvarghi, T. Manfredini, Wear behaviour of thermally sprayed ceramic oxide coatings, Wear 261 (11) (2006) 1298–1315.

[66] L.H. Tian, W. Xiong, C. Liu, S. Lu, M. Fu, Microstructure and wear behavior of atmospheric plasma-sprayed AlCoCrFeNiTi high-entropy alloy coating, J. Mater. Eng. Perform. 25 (12) (2016) 5513–5521.

[67] A. Ohmori, C.J. Li, Quantitative characterization of the structure of plasma-sprayed Al_2O_3 coating by using copper electroplating, Thin Solid Films 201

(2) (1991) 241–252.

[68] J.K. Xiao, H. Tan, Y.Q. Wu, J. Chen, C. Zhang, Microstructure and wear behavior of FeCoNiCrMn high entropy alloy coating deposited by plasma spraying, Surf. Coating. Technol. 385 (2020) 125430.

[69] H. Liu, J. Liu, P. Chen, H. Yang, Microstructure and high temperature wear behaviour of in-situ TiC reinforced AlCoCrFeNi-based high-entropy alloy composite coatings fabricated by laser cladding, Optic Laser. Technol. 118 (2019) 140–150.

[70] L.H. Tian, Z.K. Feng, W. Xiong, Microstructure, microhardness, and wear resistance of AlCoCrFeNiTi/Ni60 coating by plasma spraying, Coatings 8 (3) (2018) 13.

[71] D.A. Stewart, P.H. Shipway, D.G. McCartney, Influence of heat treatment on the abrasive wear behaviour of HVOF sprayed WC–Co coatings, Surf. Coating. Technol. 105 (1–2) (1998) 13–24.

[72] H. Liao, B. Normand, C. Coddet, Influence of coating microstructure on the abrasive wear resistance of WC/Co cermet coatings, Surf. Coating. Technol. 124 (2) (2000) 235–242.

[73] D. Lin, L. Xu, H. Jing, Y. Han, L. Zhao, F. Minami, Effects of annealing on the structure and mechanical properties of FeCoCrNi high-entropy alloy fabricated via selective laser melting, Addit. Manuf. 32 (2020) 101058.

[74] C. Samuel, M. Arivarasu, T. Ram Prabhu, High temperature dry sliding wear behaviour of laser powder bed fused Inconel 718, Addit. Manuf. 34 (2020) 101279.

[75] Y. Shi, B. Yang, X. Xie, J. Brechtl, K.A. Dahmen, P.K. Liaw, Corrosion of Al$_x$-CoCrFeNi high-entropy alloys: Al-content and potential scan-rate dependent pitting behavior, Corrosion Sci. 119 (2017) 33–45.

[76] G.T. Burstein, P.C. Pistorius, S.P. Mattin, The nucleation and growth of corrosion pits on stainless steel, Corrosion Sci. 35 (1) (1993) 57–62.

[77] W. Wang, W. Qi, L. Xie, X. Yang, J. Li, Y. Zhang, Microstructure and corrosion behavior of (CoCrFeNi)$_{95}$Nb$_5$ high-entropy alloy coating fabricated by plasma spraying, Materials 12 (5) (2019) 694.

[78] Q.H. Li, T.M. Yue, Z.N. Guo, X. Lin, Microstructure and corrosion properties of AlCoCrFeNi high entropy alloy coatings deposited on AISI 1045 steel by the electrospark process, Metall. Mater. Trans. A-Phys. Metall. Mater. Sci. 44 (4) (2013) 1767–1778.

[79] J. Liu, H. Liu, P. Chen, J. Hao, Microstructural characterization and corrosion behaviour of AlCoCrFeNiTi$_x$ high-entropy alloy coatings fabricated by laser cladding, Surf. Coating. Technol. 361 (2019) 63–74.

[80] G. Zhang, H. Liu, X. Tian, P. Chen, H. Yang, J. Hao, Microstructure and properties of AlCoCrFeNiSi high-entropy alloy coating on AISI 304 stainless steel by laser cladding, J. Mater. Eng. Perform. 29 (1) (2020) 278–288.

[81] X.W. Qiu, C.G. Liu, Microstructure and properties of Al$_2$CrFeCoCuTiNi$_x$ high-entropy alloys prepared by laser cladding, J. Alloys Compd. 553 (2013) 216–220.

[82] Y.Q. Jiang, J. Li, Y.F. Juan, Z.J. Lu, W.L. Jia, Evolution in microstructure and corrosion behavior of AlCoCrxFeNi high-entropy alloy coatings fabricated by laser cladding, J. Alloys Compd. 775 (2019) 1–14.

[83] S. Zhang, C.L. Wu, C.H. Zhang, M. Guan, J.Z. Tan, Laser surface alloying of FeCoCrAlNi high-entropy alloy on 304 stainless steel to enhance corrosion and cavitation erosion resistance, Optic Laser. Technol. 84 (2016) 23–31.

[84] R. Wang, K. Zhang, C. Davies, X. Wu, Evolution of microstructure, mechanical and corrosion properties of AlCoCrFeNi high-entropy alloy prepared by direct laser fabrication, J. Alloys Compd. 694 (2017) 971–981.

[85] Q. Ye, K. Feng, Z. Li, F. Lu, R. Li, J. Huang, Y. Wu, Microstructure and corrosion properties of CrMnFeCoNi high entropy alloy coating, Appl. Surf. Sci. 396 (2017) 1420–1426.

[86] H. Ezuber, A. El-Houd, F. El-Shawesh, A study on the corrosion behavior of aluminum alloys in seawater, Mater. Des. 29 (4) (2008) 801–805.

[87] C. Delgado-Alvarado, P.A. Sundaram, A study of the corrosion behavior of gamma titanium aluminide in 3.5 wt% NaCl solution and seawater, Corrosion Sci. 49 (9) (2007) 3732–3741.

[88] C.C. Yen, H.N. Lu, M.H. Tsai, B.W. Wu, Y.C. Lo, C.C. Wang, S.Y. Chang, S.K. Yen, Corrosion mechanism of annealed equiatomic AlCoCrFeNi tri-phase high-entropy alloy in 0.5 M H_2SO_4 aerated aqueous solution, Corrosion Sci. 157 (2019) 462–471.

[89] M. Paunovic, M. Schlesinger, Fundamentals of Electrochemical Deposition, second ed., John Wiley and Sons, 2005, p. 373.

[90] S. Khireche, D. Boughrara, A. Kadri, L. Hamadou, N. Benbrahim, Corrosion mechanism of Al, Al–Zn and Al–Zn–Sn alloys in 3wt.% NaCl solution, Corrosion Sci. 87 (2014) 504–516.

[91] J. Kawakita, T. Fukushima, S. Kuroda, T. Kodama, Corrosion behaviour of HVOF sprayed SUS316L stainless steel in seawater, Corrosion Sci. 44 (11) (2002) 2561–2581.

[92] T.E. Lister, R.N. Wright, P.J. Pinhero, W.D. Swank, Corrosion of thermal spray hastelloy C-22 coatings in dilute HCl, J. Therm. Spray Technol. 11 (4) (2002) 530–535.

[93] J.M. Guilemany, N. Cinca, S. Dosta, A.V. Benedetti, Corrosion behaviour of thermal sprayed nitinol coatings, Corrosion Sci. 51 (1) (2009) 171–180.

[94] S.D. Zhang, J. Wu, W.B. Qi, J.Q. Wang, Effect of porosity defects on the long-term corrosion behaviour of Fe-based amorphous alloy coated mild steel, Corrosion Sci. 110 (2016) 57–70.

[95] Y. Jiang, H. Tan, Z. Wang, J. Hong, L. Jiang, J. Li, Influence of Creq/Nieq on pitting corrosion resistance and mechanical properties of UNS S32304 duplex stainless steel welded joints, Corrosion Sci. 70 (2013) 252–259.